BIELEFELD UNIVERSITY

FACULTY OF PHYSICS

MASTER THESIS

The Equation of State of lattice QCD in the strong coupling regime

Dennis Bollweg

Supervisor and first Referee:
Dr. Wolfgang Unger

Second Referee:
Prof. Dr. Frithjof Karsch

Contents

1. Introduction

Since its inception, lattice gauge theory has made tremendous progress and has become a standard tool of modern high energy physics. Especially in the field of Quantum Chromodynamics, the fundamental theory of the strong interaction, lattice gauge theory is often the only method to obtain reliable predictions as perturbative methods are only applicable at very high energies. Albeit its success, there is a special class of problems where even the methods of lattice gauge theory are inhibited. At their heart, most lattice gauge theory methods are elaborate importance sampling Monte Carlo methods that use the Boltzmann weight e^{-S_E}, where S_E is the euclidean action of the system. As such, their applicability relies on the probability interpretation of e^{-S_E}. There are, however, certain cases where the action becomes complex, for example for QCD at finite density or for theories with a topological θ-term. Consequently, e^{-S_E} is no longer positive definite and cannot be used for importance sampling. This is known as the sign problem. Over the years, many interesting approaches to solve it have been proposed. Among the most promising ones are the complex Langevin method, Lefschetz thimbles and dual formulations. Complex Langevin methods has its roots in the stochastic quantization procedure. Based on a stochastic differential equation, the complexified fields are evolved in a fictious Langevin time and expectation values are obtained by averaging over the Langevin time. This method completely avoids the need for real actions but it suffers from convergence problems under certain circumstances [1]. The Lefschetz thimble approach is also based on complexifying the fields and tries to solve the sign problem by deforming the integration manifold into "thimbles" on which the phase of the Boltzmann factor is constant [2]. At the current stage, this method has only been succesfully applied to low dimensional systems. Both of these methods have in common that they are quite general and not neccesarily restricted to QCD. In contrast, the dual formulation approach is applied on a case-by-case basis and aims to transform the degrees of freedom of the physical system into a representation with positive weights, usually by rewriting them in terms of integer occupation numbers. Such a dual representation was for example found for QCD in the strong coupling limit [3],[4]. The invention of the worm algorithms for this system revived the interest in strong coupling lattice QCD [5] and recently, a lot of effort is expended towards generalizing the formulation beyond the strong coupling limit [6].

In this thesis, we want to use this dual formulation to study bulk thermodynamic properties in the T, μ-plane of strong coupling QCD which is usually prohibited by the sign problem. After introducing the formulation of QCD in the continuum and on the lattice, we will review the construction of the dual formulation and derive how observables like the energy density or the pressure can be calculated. A large part of this thesis will be concerned with the exploration of various observable across the T, μ-plane with numerical simulations. The necessary methods to do so will be developed for the simple case of massless $U(3)$ and $SU(3)$ theories at $\mu_B = 0$. From there, we will first introduce a quark mass and investigate its effect before we finally move to simulations across the full T, μ-plane. Lastly, we will use the results from this investigation to test the Taylor expansion method of the pressure that is used in conventional QCD simulations to obtain informations about the finite density region.

2. Quantum Chromodynamics

In this introductory section, we want to summarize important concepts of QCD. Based on the formulation of a classical lagrangian, we identify the underlying symmetries. We briefly introduce the path-integral quantization and discuss its influence on the classical symmetries. Lastly, we describe how the notions of temperature and chemical potential are introduced into quantum field theory and illustrate the influence of these control parameters on the behaviour of QCD matter by discussing the phase diagram.

2.1. Formulation and Symmetries

To start, we briefly recapitulate the formulation of QCD on a classical Lagrangian level. QCD is the fundamental gauge theory describing the strong force and as such, its Lagrangian specifies the behaviour of quarks and gluons and their respective interactions. The quarks (antiquarks) are described by Dirac spinors $\psi_i(x)$ $(\bar{\psi}_i(x))$, $i \in \{1,2,3\}$ belonging to the fundamental representation of $SU(3)$, the gauge group of QCD. Gluons, on the other hand, are described by the gauge fields $A^a_\mu(x), a \in \{1,2,\ldots,8\}$ and belong to the adjoint representation of $SU(3)$. The QCD Lagrangian reads

$$\begin{aligned}
&\mathcal{L}_{\mathrm{QCD}} = \mathcal{L}_{\mathrm{quarks}} + \mathcal{L}_{\mathrm{gluons}} = \sum_{f=1}^{6} \bar{\psi}_f (\mathrm{i}\not{D} - m_f)\psi_f - \frac{1}{4} F^a_{\mu\nu} F^{\mu\nu,a}, \qquad (2.1)\\
&\text{where } \not{D} = \gamma^\mu \left(\partial_\mu - \mathrm{i}g_s T^a A^a_\mu(x)\right),\\
&\text{and } F^a_{\mu\nu} = \partial_\mu A^a_\nu(x) - \partial_\nu A^a_\mu(x) - \mathrm{i}g_s f^{abc}\left[A^b_\mu(x), A^c_\nu(x)\right].
\end{aligned}$$

Here, f^{abc} are the structure constants and T^a the generators of the fundamental representation of $SU(3)$. In terms of its structure, it resembles the Lagrangian of Quantum Electrodynamics. However, there are subtle differences between the two that introduce vastly different physics. Firstly, we have six different flavors of quarks, i.e. six different masses m_f. From lightest to heaviest quark, they are labeled: up, down, strange, charm, bottom and top. Secondly, we now have eight gluons according to the eight generators of $SU(3)$ instead of one photon as in QED. And lastly, $SU(3)$ is a non-abelian group. As a consequence, there is a third term in the definition of the field strength tensor proportional to the commutator $\left[A^b_\mu(x), A^c_\nu(x)\right]$. This term is responsible for the introduction of gluon self-interactions, as $F^a_{\mu\nu}F^{\mu\nu,a}$ now contains terms with cubic and quartic powers of A^a_μ.
By construction, this Lagrangian is locally gauge invariant. That is, it is invariant under transformations $U \in SU(3)$, $U = \mathrm{e}^{-\mathrm{i}T^a\Theta^a(x)}$, where the fields transform as

$$\psi(x) \to \psi'(x) = \mathrm{e}^{-\mathrm{i}T^a\Theta^a(x)}\psi(x), \qquad (2.2)$$

$$T^a A^a_\mu(x) \to T^a A'^a_\mu(x) = U(x)\left(T^a A^a_\mu(x) - \frac{\mathrm{i}}{g_s} U(x)^{-1}\partial_\mu U(x)\right)U(x)^{-1}. \qquad (2.3)$$

Additionally, $\mathcal{L}_{\mathrm{QCD}}$ posseses a number of continuous global symmetries which are linked to conserved charges by Noether's theorem. A simple example that is readily seen is a global

$U(1)$ symmetry. Transforming the quarks according to

$$\psi \to \psi' = \mathrm{e}^{\mathrm{i}\phi}\psi,$$

where ϕ is a constant, does not change $\mathcal{L}_{\text{quarks}}$ because the exponentials are cancelled by their conjugated counterparts coming from $\bar{\psi}$. The conserved charge corresponding to this symmetry is the baryon number. This global complex phase can be embedded in a larger symmetry group, provided that some of the quark masses are degenerate. We assume this is the case for n quarks with mass m. Then by adopting a vector notation for the flavor space

$$\mathcal{L}_{\text{deg.}} = \sum_{f=1}^{n} \bar{\psi}_f \left(\mathrm{i}\not{D} - m_f\right) \psi_f = \bar{\Psi} \left(\mathrm{i}\not{D}\mathbb{1} - M\right) \Psi$$

$$\text{with } \Psi = \begin{pmatrix} u \\ d \\ \vdots \end{pmatrix} \text{ and } M = \operatorname{diag}(m, \ldots, m),$$

we can see that unitary transformations $\Omega \in U(n)$ on that subset of the flavor space form a symmetry of $\mathcal{L}_{\text{quarks}}$. Moreover, since $U(n) = U(1) \times SU(n)$ we can decompose these transformations into $\Omega = \mathrm{e}^{-i\phi}\Lambda$ with $\Lambda \in SU(n)$. As $m_u \approx m_d$, n is often set to 2 in practical applications. Furthermore, we can use the projection operators $P_{R/L} = \frac{1}{2}\left(\mathbb{1} \pm \gamma^5\right)$ to separate the quark fields into left-handed and right-handed components. Now we use $P_{\mathrm{R}} + P_{\mathrm{L}} = 1$ to write $\psi = \left(P_{\mathrm{R}} + P_{\mathrm{L}}\right)\psi = \psi_{\mathrm{R}} + \psi_{\mathrm{L}}$. Since $P_{\mathrm{R}}P_{\mathrm{L}} = P_{\mathrm{L}}P_{\mathrm{R}} = 0$ and $\{\gamma^\mu, \gamma^5\} = 0$, applying this separation to $\mathcal{L}_{\text{quarks}}$ leads to

$$\begin{aligned}
\mathcal{L}_{\text{deg.}} &= \sum_{f=1}^{n} \bar{\psi}_f \left(\mathrm{i}\not{D} - m_f\right) \psi_f \\
&= \sum_{f=1}^{n} \bar{\psi}_{\mathrm{R},f}\mathrm{i}\not{D}\psi_{\mathrm{R},f} + \bar{\psi}_{\mathrm{L},f}\mathrm{i}\not{D}\psi_{\mathrm{L},f} - m_f \left(\bar{\psi}_{\mathrm{R},f}\psi_{\mathrm{L},f} + \bar{\psi}_{\mathrm{L},f}\psi_{\mathrm{R},f}\right).
\end{aligned}$$

Thus, if $m_f = 0$ for $f \in \{1, \ldots, n\}$ the symmetry of $\mathcal{L}_{\text{quarks}}$ can be extended further by transforming left-handed and right-handed components independently. This so-called chiral symmetry can then be written as $U_{\mathrm{R}}(n) \times U_{\mathrm{L}}(n) = U(1) \times U_A(1) \times SU_{\mathrm{R}}(n) \times SU_{\mathrm{L}}(n)$, where $U_A(1)$ denotes the axial symmetry that transforms the fields via

$$\begin{aligned}
\psi &\to \psi' = \mathrm{e}^{\mathrm{i}\alpha\gamma^5}\psi \\
\bar{\psi} &\to \bar{\psi}' = \bar{\psi}\mathrm{e}^{\mathrm{i}\alpha\gamma^5}.
\end{aligned}$$

The equal signs in the exponentials of the transformation law ensure invariance of the $\not{D}$ terms because $\{\gamma^\mu, \gamma^5\} = 0$ but a non-zero mass explicitly breaks this symmetry:

$$\begin{aligned}
\bar{\psi}\gamma^\mu\psi \to \bar{\psi}'\gamma^\mu\psi' &= \bar{\psi}\mathrm{e}^{\mathrm{i}\alpha\gamma^5}\gamma^\mu\mathrm{e}^{\mathrm{i}\alpha\gamma^5}\psi = \bar{\psi}\mathrm{e}^{\mathrm{i}\alpha\gamma^5}\mathrm{e}^{-\mathrm{i}\alpha\gamma^5}\psi = \bar{\psi}\gamma^\mu\psi \\
\bar{\psi}\psi \to \bar{\psi}'\psi' &= \bar{\psi}\mathrm{e}^{2\mathrm{i}\alpha\gamma^5}\psi \neq \bar{\psi}\psi.
\end{aligned}$$

For QCD in the chiral limit, i.e. $m_f = 0 \ \forall f$, there exists a further symmetry called the conformal symmetry which is related to the scale invariance of the theory[1]. Its associated symmetry transformations change a general field ϕ via

$$\phi(x) \to \mathrm{e}^{-D\sigma}\phi(x\mathrm{e}^{-\sigma}),$$

where D is the mass dimension of the field ϕ. The corresponding Noether current $D^\mu(x)$ is related to the symmetrised energy-momentum tensor $\Theta^{\mu\nu}$ [7]

$$D^\mu = \Theta^{\mu\nu}x_\nu. \tag{2.4}$$

The conservation law for Noether currents then implies

$$\partial_\mu D^\mu = \partial_\mu\Theta^{\mu\nu}x_\nu = \delta_{\mu\nu}\Theta^{\mu\nu} + x_\nu\partial_\mu\Theta^{\mu\nu} = \Theta^\mu_\mu \stackrel{!}{=} 0$$

In the massive case, we have

$$\Theta^\mu_\mu = m\bar{\psi}\psi. \tag{2.5}$$

2.2. Quantization

To move towards a quantum field theory of strong interactions, we need to quantize the above classical theory. One possible variant, and the most convenient for a lattice discretization, is the path-integral formulation. For a generic scalar field theory with classical Lagrangian $\mathcal{L}$ and fields ϕ, the n-point function $G_n(x_1,\ldots,x_n)$ is given by

$$G_n(x_1,\ldots,x_n) = \langle 0|T\{\hat{\phi}(x_1),\ldots,\hat{\phi}(x_n)\}|0\rangle = \frac{\int \mathcal{D}\phi\ \phi(x_1)\cdots\phi(x_n)\mathrm{e}^{\mathrm{i}S[\phi]}}{\int \mathcal{D}\phi\ \mathrm{e}^{\mathrm{i}S[\phi]}},$$

where $\int \mathcal{D}\phi$ denotes, figuratively, the integration over all admissable functional forms of the fields ϕ and $S[\phi] = \int \mathrm{d}^4x\mathcal{L}$ is the classical action. $G_n(x_1,\ldots,x_n)$ is also proportional to the n-th functional derivative of the generating functional

$$Z[J] = \int \mathcal{D}\phi\ \mathrm{e}^{\mathrm{i}S + \int \mathrm{d}^4x\ J(x)\phi(x)}.$$

There are some subtleties in formulating this path-integral; particularly so for non-abelian gauge theories. For a purely gluonic theory, the naive approach

$$Z[J] = \int \mathcal{D}A\mathrm{e}^{\mathrm{i}S[A^a_\mu] + \int \mathrm{d}^4x J^{a,\mu}A^a_\mu}$$

has to be suplemented with a gauge-fixing condition $G^\mu A^a_\mu = B^a$ in order to be well-defined. This condition can be implemented by modifying the integration measure

$$\mathcal{D}A \to \mathcal{D}A \det\left(\frac{\delta(G^\mu A'^a_\mu(x))}{\delta\theta^b(y)}\right)\prod_{a,x}\delta(G^\mu A^a_\mu(x) - B^a(x)).$$

[1] In chiral QCD, all coupling constants in $\mathcal{L}$ have mass dimension 0.

The δ-function can also be absorbed in the Lagrangian by functional integration over $B^a(x)$ with the weight

$$\exp\left\{-\frac{1}{2\alpha}\int \mathrm{d}^4x\ (B^a)^2\right\}.$$

Correctly, $Z[J]$ then reads

$$Z[J] = \int \mathcal{D}A \det\left(\frac{\delta(G^\mu A'^a_\mu(x))}{\delta\theta^b(y)}\right) \exp\left\{\mathrm{i}\int \mathrm{d}^4x\ \left(\mathcal{L} - \frac{1}{2\alpha}(G^\mu A^a_\mu(x))^2 + J^{a,\mu}A^a_\mu\right)\right\}.$$

Note that for usage in perturbation theory, the determinant may be written in terms of a Faddeev-Popov ghosts by introducing auxilliary fields.
The path-integral for the fermionic part of $\mathcal{L}_{\mathrm{QCD}}$ also faces difficulties. To find a sensible definition, the anti-commuting nature of fermions has to be reconciled with the classical fields. This is done by introducing fermion fields $\bar\psi$ and ψ as anti-commuting, complex Grassmann numbers. The generating functional of fermions may then be written as

$$\begin{aligned} Z[J,\bar J] &= \int \mathcal{D}\psi\mathcal{D}\bar\psi \exp\left\{i\int \mathrm{d}^4x\left(\mathcal{L} + \bar\psi J + \bar J\psi\right)\right\}, \\ &\text{with}\quad \left\{\psi(x),\bar\psi(y)\right\} = 0,\ \left\{\psi(x),J(y)\right\} = 0,\quad \text{etc.} \end{aligned}$$

In total, we have

$$Z[J,J_F,\bar J_F] = \int \mathcal{D}A \int \mathcal{D}\psi\mathcal{D}\bar\psi \det\left(\frac{\delta(G^\mu A'^a_\mu(x))}{\delta\theta^b(y)}\right) \tag{2.6}$$

$$\times \exp\left\{\mathrm{i}\int \mathrm{d}^4x\ \left(\mathcal{L}_{\mathrm{QCD}} - \frac{1}{2\alpha}(G^\mu A^a_\mu(x))^2 + J^{a,\mu}A^a_\mu + \bar\psi J_F + \bar J_F\psi\right)\right\}. \tag{2.7}$$

Expectation values of general observables $\mathcal{O}$ are then obtained by

$$\langle\mathcal{O}\rangle = \frac{\int\mathcal{D}A\int\mathcal{D}\psi\mathcal{D}\bar\psi\det\left(\frac{\delta(G^\mu A'^a_\mu(x))}{\delta\theta^b(y)}\right)\mathcal{O}[A,\psi,\bar\psi]\exp\left\{\mathrm{i}\int\mathrm{d}^4x\ \left(\mathcal{L}_{\mathrm{QCD}} - \frac{1}{2\alpha}(G^\mu A^a_\mu(x))^2\right)\right\}}{\int\mathcal{D}A\int\mathcal{D}\psi\mathcal{D}\bar\psi\det\left(\frac{\delta(G^\mu A'^a_\mu(x))}{\delta\theta^b(y)}\right)\exp\left\{\mathrm{i}\int\mathrm{d}^4x\ \left(\mathcal{L}_{\mathrm{QCD}} - \frac{1}{2\alpha}(G^\mu A^a_\mu(x))^2\right)\right\}}. \tag{2.8}$$

2.3. Anomalies

At this point, one may ask whether or not the classical symmetries carry over to the quantized theory. Symmetries for which this is not the case are said to be broken by a quantum anomaly. QCD in the chiral limit posseses two such anomalously broken symmetries, the axial symmetry $U_A(1)$ and the conformal symmetry. In the former case, the integration measure changes under $U_A(1)$ transformations according to

$$\begin{aligned} &\mathcal{D}\psi\mathcal{D}\bar\psi \to \mathcal{D}\psi\mathcal{D}\bar\psi\det(C)^{-2}, \\ &\text{with}\quad \det(C)^{-2} = \exp\left\{i2\alpha\int\mathrm{d}^4x\frac{\mathrm{Tr}\left[F_{\mu\nu}\tilde F_{\mu\nu}\right]}{32\pi^2}\right\} = \exp\left\{-\mathrm{i}2\alpha Q_A\right\}. \end{aligned}$$

A proof of this relation can be found in [8]. Here, we can see that gauge configurations with a topological charge $Q_A \neq 0$ introduce $\det(C) \neq 1$ and break the $U_A(1)$ symmetry. Consequently, the conservation law for the axial current is modified by

$$\partial_\mu J_A^\mu(x) = -\frac{g^2}{16\pi^2} F^{\mu\nu}(x)\tilde{F}_{\mu\nu}(x).$$

In the latter case, the anomalous breaking of conformal symmetry is obtained from simple renormalization group theory arguments. Considering chiral QCD at a different scale implies a shift in the renormalized coupling $g_s \to g_s + \sigma\beta(g_s)$, such that the Lagrangian[2] is modified by

$$\delta\mathcal{L} = \sigma\beta(g_s)\frac{\partial}{\partial g_s}\mathcal{L} = \sigma\beta(g_s)\frac{\partial}{\partial g_s}\frac{-1}{4g_s^2}F^a_{\mu\nu}F^{\mu\nu,a} = \frac{\sigma\beta(g_s)}{2g_s^3}F^a_{\mu\nu}F^{\mu\nu,a}.$$

Therefore, the conservation law for the dilatation current $D^\mu(x)$ and consequently the trace of the energy-momentum tensor is modified according to

$$\Theta^\mu_\mu = \partial_\mu D^\mu \sim \beta(g_s)F^a_{\mu\nu}F^{\mu\nu,a}. \tag{2.9}$$

This is known as the trace anomaly [7].

[2]Note that we have rescaled the gauge fields $g_s T_a A^\mu_a \to T_a A^\mu_a$ so that the coupling within the covariant derivative is cancelled.

2.4. Temperature and density

So far, we have discussed the formulation of QCD and its symmetries on both a classical and quantized level. We briefly explained, how to quantize the theory with the path-integral formalism and observed the influence of quantum phenomena on the classical symmetries. Our next goal is to expand this formalism and include the concept of temperature and density and observe the link between thermodynamics and the remaining symmetries of QCD. To include a temperature into a quantum field theory, we make use of the following formal similarity between the partition function of a thermodynamical system and the generating functional for Green's functions. Given a system with Hamiltonian $\hat{H}$, the canonical partition function at temperature $T = \frac{1}{\beta}$ is given by

$$Z(\beta) = \mathrm{Tr}\ \mathrm{e}^{-\beta\hat{H}},$$

and expectation values are obtained via

$$\langle \mathcal{O} \rangle_\beta = \frac{1}{Z(\beta)} \mathrm{Tr}\ \mathcal{O} \mathrm{e}^{-\beta\hat{H}}.$$

This can be expressed in the path-integral formalism by performing a Wick rotation to imaginary time $t \to i\tau$, thereby changing to a Euclidean metric, and by restricting the τ-integral in S_E to the interval $[0, \beta]$, such that

$$Z(\beta) = \int \mathcal{D}\phi\ \mathrm{e}^{-\int_0^\beta \mathrm{d}\tau \int \mathrm{d}^3x \mathcal{L}_\mathrm{E}} = \int \mathcal{D}\phi\ \mathrm{e}^{-S_\mathrm{E}},$$

where the fields ϕ now satisfy periodic[3] boundary conditions in temporal direction $\phi(\tau = 0) = \phi(\tau = \beta)$. Expectation values at inverse temperature β are then given by

$$\langle \mathcal{O} \rangle_\beta = \frac{1}{Z(\beta)} \int \mathcal{D}\phi\ \mathcal{O}\ \mathrm{e}^{-S_\mathrm{E}}.$$

A finite density is introduced by changing to the grand-canonical ensemble with the introduction of a chemical potential μ and the particle-number operator. For the case of fermions, this is done by changing $\mathcal{L}_\mathrm{E}$ to

$$\mathcal{L}_\mathrm{E}(0) \to \mathcal{L}_\mathrm{E}(\mu) = \mathcal{L}_\mathrm{E}(0) - \mu\bar{\psi}\gamma^0\psi.$$

2.5. Phase diagram

Now that we have introduced temperature and chemical potential to our system, we may ask, how the properties of QCD matter change as a function of these two control parameters. Among the most interesting is the observation that quark matter undergoes a phase transition from a hadronic system at low temperatures to a plasma of quasi-free quarks and gluons. This is the so-called deconfinement transition. Furthermore, there is the chiral transition, across

[3] Fermions satisfy anti-periodic boundary conditions here.

which the pions, the goldstone-bosons of the chiral symmetry, become effectively massless. There also exists a nuclear transition at small temperatures and high densities which separates the hadronic phase from the nuclear matter phase. Unfortunately, the finite density region of full QCD is not accessible and we cannot show a phase diagram for this case. Instead, we will review the phase diagram that is relevant to this work: The phase diagram of QCD in the strong coupling limit. It was succesfully calculated in the massless case in [9] and is shown in Fig. 1 below.

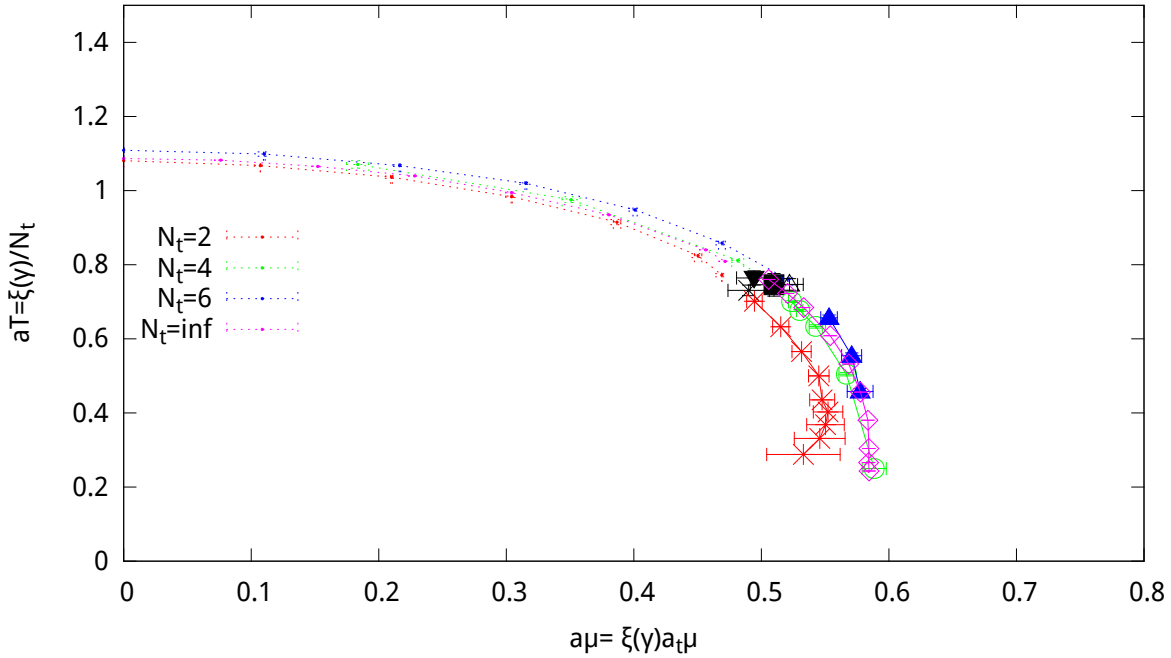

Figure 1: The phase diagram of strong coupling lattice QCD. The dotted line represents the second order transition, the black data points correspond to the tri-critical point and the full line corresponds to the first order transition.

The strong coupling limit cannot adress deconfinement phenomena as the quarks are always confined into color-singlet degrees of freedom. The chiral and nuclear transitions are nonetheless still accessible. In the massless case, the phase diagram consists of a second order line that extends from $\mu = 0$ to $\mu_c \sim 0.5$. Above the second order line, the chiral condensate, the order parameter of the chiral symmetry, vanishes. Below the line, chiral symmetry is spontaneously broken and the chiral condensate possesses a non-zero value. At μ_c, a tri-critical point seperates the second order line from the first order line. Interestingly, the chiral first order line coincides with the first order nuclear transition. The latter does not have a second order line for $\mu < \mu_c$ but terminates in a second order critical endpoint. For finite quark masses, the second order chiral transition turns into a smooth crossover. The quark mass dependence of the critical endpoint was studied in [10].

3. QCD on the lattice

A major obstacle in understanding QCD is its strong coupling for small and intermediate energy scales. It spoils convergence of any perturbative expansion of (2.8) and non-perturbative methods are needed instead. The most prominent non-perturbative method is the lattice discretization which we want to describe in the following. The central idea is to discretize spacetime such that path-integrals become finite-dimensional and can be evaluated numerically. The continuum theory can later be obtained by extrapolating from calculations at different lattice spacings, while keeping the physical extent of the system fixed.

3.1. Discretizing the fermion action

We start by discretizing S_{E} for free quarks: we replace derivatives by central differences

$$\partial_\mu \psi(x) \to \frac{\psi(x+\hat{\mu}) - \psi(x-\hat{\mu})}{2a} \tag{3.1}$$

and introduce a fundamental lattice spacing a. The quark fields are now defined on the lattice sites $x \in \Lambda$ with

$$\Lambda = \{x = (x_0, \ldots, x_3) | x_0 = 0, 1, \ldots, N_\tau - 1, x_i = 0, 1, \ldots, N_\sigma - 1\}\,. \tag{3.2}$$

The fields are periodic in spatial and anti-periodic in temporal direction. Our physical four-volume V_4 is now given as $V_4 = a^4 N_\sigma^3 N_\tau$ and N_σ and N_τ denote the number of spatial and temporal lattice sites. The integral over the four-volume is replaced by a sum over all lattice sites x

$$\int \mathrm{d}^4 x \to a^4 \sum_{x \in \Lambda}, \tag{3.3}$$

so that we obtain

$$S_{\mathrm{free}} = a^4 \sum_{x \in \Lambda} \left(\sum_{\mu=0}^{3} \bar{\psi}(x) \frac{\gamma^\mu}{2a} \left(\psi(x+\hat{\mu}) - \psi(x-\hat{\mu}) \right) \right) + m \bar{\psi}(x) \psi(x). \tag{3.4}$$

To include gauge fields, we can make use of the definition of the covariant derivative using a comparator $U(y,x)$. In the continuum, one defines

$$n^\mu D_\mu f(x) = \lim_{\epsilon \to 0} \frac{f(x+\epsilon n) - U(x+\epsilon n, x) f(x)}{\epsilon},$$

with the transformation property $U(y,x) \to V(y) U(y,x) V(x)^\dagger$ under gauge transformations $V \in SU(3)$. For infinitesimal ϵ, it is related to the gauge field $A_\mu(x)$ via

$$U(x+\epsilon n, x) = 1 + i g_s \epsilon n^\mu A_\mu^a T^a + \mathcal{O}(\epsilon^2).$$

Analogously, we discretize the covariant derivative by introducing the link variables $U_\mu(x) \in SU(3)$ such that

$$D_\mu \psi(x) \to \frac{U_\mu(x)\psi(x+\hat{\mu}) - U_{-\mu}(x)\psi(x-\hat{\mu})}{2a}. \tag{3.5}$$

Finally, the so-called naive fermion action reads

$$S_{\text{naive}} = a^4 \sum_{x\in\Lambda} \bar{\psi}(x) \frac{\gamma^\mu}{2a} \left(U_\mu(x)\psi(x+\hat{\mu}) - U_{-\mu}(x)\psi(x-\hat{\mu})\right) + m\bar{\psi}(x)\psi(x). \tag{3.6}$$

The particle content described by the above action can be obtained from the poles of the corresponding quark propagator in momentum space. Physically, the pole is located at $p^2 = m^2$. For the naive action, however, there are 15 additional unphysical poles located at the corners of the first Brillouin zone. The appearance of such unphysical poles is called doubling problem. Fortunately, the discretization procedure is by no means unique and one may construct different discretization schemes that remove these unphysical poles or reduce their number. From now on, we will focus on the so-called staggered fermions. They reduce the number of doublers from 16 to four while also leaving chiral symmetry intact. With respect to strong coupling expansions, their structure gives rise to exactly solvable link-integrals, which will be discussed later. They are obtained from the naive action by diagonalizing the Dirac matrices, such that the different Dirac components of the new fields ψ decouple. Mathematically, we are searching for transformations

$$\psi(x) \to \psi'(x) = A_x \psi(x), \quad \bar{\psi}(x) \to \bar{\psi}'(x) = \bar{\psi}(x) A_x^\dagger,$$

such that

$$A_x^\dagger \gamma_\mu A_{x+\hat{\mu}} = \Delta_\mu(x) \in U(1)^{\otimes 4}, \tag{3.7}$$

where $\Delta_\mu(x)$ is diagonal and unitary. A common choice for the transformation matrices $A_\mu(x)$ that satisfies (3.7) is given by

$$\begin{aligned} \bar{\psi}(x) &\to \bar{\psi}(x) \gamma_3^{x_3} \gamma_2^{x_2} \gamma_1^{x_1} \gamma_0^{x_0} \\ \psi(x) &\to \gamma_0^{x_0} \gamma_1^{x_1} \gamma_2^{x_2} \gamma_3^{x_3} \psi(x). \end{aligned} \tag{3.8}$$

Since $\{\gamma_i, \gamma_j\} = 2\delta_{i,j}\mathbb{1}$, the mass term is invariant under (3.8), but the derivative term obtains a factor of

$$\eta_\mu(x) = (-1)^{\sum_{\nu<\mu} x_\nu}, \tag{3.9}$$

the so-called staggered phases. As the different Dirac components are decoupled, we can restrict us to only one of the components of the Dirac spinor and discard the other three. This reduces the number of doublers from 16 to 4. The resulting quark action then reads

$$S_{\text{stag.}} = a^4 \sum_{x\in\Lambda} \bar{\psi}(x) \frac{\eta^\mu(x)}{2a} \left(U_\mu(x)\psi(x+\hat{\mu}) - U_{-\mu}(x)\psi(x-\hat{\mu})\right) + m\bar{\psi}(x)\psi(x). \tag{3.10}$$

3.2. Discretizing the gauge action

We have introduced the gauge fields via parallel transporters $U_\mu(x)$ to promote the standard derivative to a covariant version as required by gauge invariance. Now, we need to introduce an action for the link variables themselves. For that purpose, we choose the well-known Wilson gauge action

$$S_{\text{Wilson}} = \frac{\beta_G}{2N_c} \sum_P \text{Tr}\left(U_P + U_P^\dagger\right), \tag{3.11}$$

where the sum is over all elementary plaquettes $P = (x, \mu, \nu)$ spanned by going from site x to the neighboring sites $x + \hat{\mu}$ and $x + \hat{\nu}$ and

$$U_P = U_{\mu,\nu}(x) = U_\mu(x)U_\nu(x + \hat{\mu})U_{-\mu}(x + \hat{\mu} + \hat{\nu})U_{-\nu}(x + \hat{\nu}). \tag{3.12}$$

3.3. Temperature on the lattice

With the introduction of temperature in section 3, the temporal direction attracted some special attention, as its extent is directly linked to the temperature of the quantum field theory. By comparing the lattice expressions to the continuum versions, we see that temperature on the lattice can be identified via

$$\beta = aN_\tau \;\text{ or }\; aT = \frac{1}{N_\tau}. \tag{3.13}$$

Thus, to vary the temperature, one has to vary either the lattice spacing a or the temporal extent N_τ. Of course, the latter can only be changed discretely so it is common to set the temperature with the help of the lattice spacing. After setting the scale[4], the lattice spacing $a = a(\beta_G)$ can be varied by changing the inverse gauge coupling β_G. For the purpose of this thesis, this common method is unfortunately not applicable. Our calculations are performed in the strong coupling limit $\beta_G \to 0$ and therefore the inverse gauge coupling can not be varied. Changing the temperature discretely by N_τ is also insufficient because the highest temperature accesible with this method is $aT = \frac{1}{2}$ and the chiral phase transition in strong coupling QCD appears at roughly $aT \sim 1$. Consequently, much of the interesting physical phenomena would not be accessible with this method. To aleviate this, we further deepen the contrast of temporal and spatial directions by introducing an anisotropic lattice with lattice spacing a_τ in temporal direction and a in spatial direction. If we define the physical anisotropy $\xi = \frac{a}{a_\tau}$, we can write

$$\beta = a_\tau N_\tau \Rightarrow aT = \frac{a}{a_\tau N_\tau} = \frac{\xi}{N_\tau}. \tag{3.14}$$

On anisotropic lattices, we can therefore vary aT continously given that we find a way to set the physical anisotropy ξ. For that purpose, we introduce the additional parameter γ, the bare

[4]This can be done, for example, by using the sommer parameter or by comparing hadron masses on the lattice to experimental data.

anisotropy coupling, to our lattice action [9]. For staggered fermions the anisotropic action reads

$$S_{\text{stag.}} = a_\tau a^3 \sum_{x\in\Lambda} \bar{\psi}(x) \left(\frac{\gamma\eta^0(x)}{2a_\tau} \left(U_0(x)\psi(x+\hat{0}) - U_{-0}(x)\psi(x-\hat{0}) \right) \right. \tag{3.15}$$

$$\left. + \frac{\eta^i(x)}{2a} \left(U_i(x)\psi(x+\hat{i}) - U_{-i}(x)\psi(x-\hat{i}) \right) \right) + m\bar{\psi}(x)\psi(x), \tag{3.16}$$

and $\gamma > 1$ favors temporal quark hoppings over spatial ones.

3.4. Chemical potential on the lattice

The last ingredient to translate the continuum theory to the lattice is to introduce the chemical potential. In the continuum Lagranian, it multiplies the conserved charge of the $U(1)$ flavor symmetry. Its operator reads

$$\hat{Q}_B = \int \mathrm{d}^3x \bar{\psi}(x)\gamma_0\psi(x).$$

As pointed out by Karsch and Hasenfratz in [11], directly translating this operator onto the lattice leads to divergencies in the energy density even for free quarks. Instead, they proposed to modify temporal hoppings by

$$S = a_\tau a^3 \sum_{x\in\Lambda} \left(\bar{\psi}(x) \left(\frac{\gamma\eta^0(x)}{2a_\tau} \mathrm{e}^{a_\tau\mu} U_0(x)\psi(x+\hat{0}) - \mathrm{e}^{-a_\tau\mu} U_{-0}(x)\psi(x-\hat{0}) \right) \right. \tag{3.17}$$

$$\left. + \frac{\eta^i(x)}{2a} \left(U_i(x)\psi(x+\hat{i}) - U_{-i}(x)\psi(x-\hat{i}) \right) \right) + m\bar{\psi}(x)\psi(x).$$

The presence of a chemical potential thus favors temporal forward hoppings over backwards hoppings, in contrast to the anisotropy which favors temporal hoppings regardless of the orientation.

3.5. Lattice partition function

Summarizing the above points, we now formulate the partition function at finite T and μ as a lattice path integral. As above, the degrees of freedom of our lattice theory are the quark fields $\bar{\psi}(x)$ and $\psi(x)$ and the link variables $U_\mu(x)$. The measures for lattice path integration in these variables reads

$$\mathcal{D}\psi = \prod_{x\in\Lambda} \mathrm{d}\psi(x) \quad \mathcal{D}U = \prod_{x\in\Lambda} \prod_{\mu=0}^{3} \mathrm{d}U_\mu(x),$$

where $\mathrm{d}\psi(x)$ is the measure for integrating grassmann-numbers and $\mathrm{d}U_\mu(x)$ is the Haar measure. $\mathrm{d}\psi(x)$ fulfills

$$\mathrm{d}\psi_i \mathrm{d}\psi_j = -\mathrm{d}\psi_j \mathrm{d}\psi_i,$$
$$\int \mathrm{d}\psi\ \psi = 1, \quad \int \mathrm{d}\psi = 0.$$

The Haar measure $\mathrm{d}U_\mu(x)$ is invariant under group multiplication

$$\int_G f(U)\mathrm{d}U = \int_G f(VU)\mathrm{d}U \quad \text{for} \quad V \in SU(3).$$

The partition function can be written as a lattice path integral by combining the above remarks to obtain

$$\begin{aligned} Z(T,\mu) &= \int \mathcal{D}U \int \mathcal{D}\psi\mathcal{D}\bar{\psi}\mathrm{e}^{-S_\mathrm{f}-S_\mathrm{g}} \\ &= \int_{SU(3)} \int_\psi \prod_{x\in\Lambda}\prod_{\mu=0}^{3} \mathrm{d}U_\mu(x)\mathrm{d}\psi(x)\mathrm{d}\bar{\psi}(x) \;\; \mathrm{e}^{-S_\mathrm{f}[\bar{\psi},\psi,U]-S_\mathrm{g}[U]}. \end{aligned} \tag{3.18}$$

4. The strong coupling regime

While the last chapter introduced the formulation of QCD on the lattice, this chapter focuses on setting the stage for actual numerical simulations by deriving a suitable representation for efficient Monte-Carlo sampling. As a motivation, we recapitulate the source of the sign problem at finite density as it is faced in conventional QCD simulations. Then, we will derive the dual representation of strong-coupling QCD as a method to ameliorate the sign problem.

4.1. The finite density sign problem

To discuss the conventional approach to evaluate (3.18), we rewrite the partition function by making use of the bilinearity in the fermionic part of the action:

$$Z(T,\mu) = \int \mathcal{D}U \int \mathcal{D}\psi\mathcal{D}\bar{\psi} \exp\left(-\sum_x \bar{\psi} D[U]\psi\right) \mathrm{e}^{-S_\mathrm{g}[U]} = \int \mathcal{D}U \det(D[U])\ \mathrm{e}^{-S_\mathrm{g}[U]},$$

where D is the Dirac matrix originating from rewriting (3.17) with the help of Kronecker δ's. In this formulation, fermions are integrated out and the only remaining degrees of freedom are the link variables $U_\mu(x)$. Given that $\det(D[U])$ is well-behaved, $\det(D[U])\mathrm{e}^{-S_\mathrm{g}[U]}$ defines a joint probability distribution that can then be used to generate gauge configurations in importance sampling Monte-Carlo. For this to be the case, the fermion determinant has to be real and non-negative. The former is ensured given that the fermion matrix satisfies γ^5-hermiticity

$$D^\dagger = \gamma^5 D \gamma^5, \tag{4.1}$$

because then

$$\det(D) = \det(\gamma^5)\det(D)\det(\gamma^5) = \det(\gamma^5 D\gamma^5) = \det(D^\dagger) = \det(D)^*.$$

In the presence of a chemical potential, (4.1) is modified

$$D^\dagger(-\mu) = \gamma^5 D(\mu)\gamma^5,$$

and the fermion determinant becomes complex such that importance sampling is no longer applicable.

4.2. Dual representation at $\beta_G = 0$

For the remainder of this thesis, we want to use the dual representation of strong coupling lattice QCD where matter and gauge fields are integrated out to obtain a representation in terms of integer occupation numbers. The sign problem of the resulting representation is drastically reduced, such that simulations across the T,μ-plane are feasible. To start, we observe that by taking the strong coupling limit $\beta_G \to 0$ of (3.18), the gauge part of the action vanishes and

the link integration $\mathrm{d}U_\mu(x)$ factorizes:

$$\lim_{\beta_G\to 0} Z(T,\mu) = Z_{SC}(T,\mu) = \int_{SU(N_c)}\int_\psi \prod_{x\in\Lambda}\prod_{\mu=0}^{3}\mathrm{d}U_\mu(x)\mathrm{d}\psi(x)\mathrm{d}\bar\psi(x)\ \ \mathrm{e}^{-S_\mathrm{f}[\bar\psi,\psi,U]}$$

$$= \int_\psi \prod_{x\in\Lambda}\mathrm{d}\psi(x)\mathrm{d}\bar\psi(x)\mathrm{e}^{2am_q\bar\psi\psi}\int_{SU(N_c)}\prod_{\mu=0}^{3}\mathrm{d}U_\mu \mathrm{e}^{\gamma^{\delta_{0,\mu}}\eta^\mu(x)\bar\psi(x)\left(U_\mu(x)\mathrm{e}^{\delta_{\mu,0}a_\tau\mu}\psi(x+\hat\mu)-U_\mu^\dagger(x)\mathrm{e}^{-\delta_{\mu,0}a_\tau\mu}\psi(x-\hat\mu)\right)}$$

$$= \int_\psi \prod_{x\in\Lambda}\mathrm{d}\psi(x)\mathrm{d}\bar\psi(x)\mathrm{e}^{2am_q\bar\psi\psi}\prod_{\mu=0}^{3} z(x,x\pm\hat\mu), \tag{4.2}$$

where $z(x,y)$ is the one-link integral of the form

$$z(x,y) = \int_{SU(N_c)}\mathrm{d}g\ \mathrm{e}^{\mathrm{Tr}(m^\dagger g + m g^\dagger)}$$

$$\text{with}\ \ (m)_{ij} = \gamma^{\delta_{0,\mu}}\eta^\mu(x)\mathrm{e}^{\delta_{0,\mu}a_\tau\mu}\psi(x)_i\bar\psi(y)_j,\ \ (m^\dagger)_{ij} = -\gamma^{\delta_{0,\mu}}\eta^\mu(x)\mathrm{e}^{-\delta_{0,\mu}a_\tau\mu}\psi(y)_i\bar\psi(x)_j.$$

These matrices transform under gauge transformations like

$$(m)_{ij}\to(m)_{kl}U(x)_{ik}U^\dagger(y)_{lj},\ \ (m^\dagger)_{ij}\to(m^\dagger)_{kl}U(y)_{ik}U^\dagger(x)_{lj}.$$

Therefore, traces of powers of $mm^\dagger$ and determinants of m and $m^\dagger$ are gauge invariant:

$$\mathrm{Tr}\left[\left(m'(m')^\dagger\right)^n\right] = \mathrm{Tr}\left[\left(U(x)mU^\dagger(y)U(y)m^\dagger U(x)^\dagger\right)^n\right] = \mathrm{Tr}\left[\left(mm^\dagger\right)^n\right],$$
$$\det m' = \det\left(U(x)mU^\dagger(y)\right) = \det U(x)\det m\det U^\dagger(y) = \det m.$$

Since objects in the trivial representation of $SU(N_c)$ are the only contributors to the integral in $z(x,y)$, we may write

$$z(x,y) = \sum_{k_1,\ldots,k_{N_c}}\alpha_{k_1,\ldots,k_{N_c}}(\det m)^{k_1}(\det m^\dagger)^{k_2}\mathrm{Tr}\left[mm^\dagger\right]^{k_3}\cdots\mathrm{Tr}\left[\left(mm^\dagger\right)^{N_c-1}\right]^{k_{N_c+1}}. \tag{4.3}$$

Now, we define mesonic fields $M(x)$ and baryonic fields $B(x)$ by

$$M(x) = \psi_i(x)\bar\psi_i(x),\ \ B(x) = \frac{1}{N_c!}\epsilon_{i_1,\ldots,i_{N_c}}\psi_{i_1}(x)\cdots\psi_{i_{N_c}}(x), \tag{4.4}$$

and make use of the identifications

$$\mathrm{Tr}\left[\left(mm^\dagger\right)^n\right] = (-1)^{n+1}M(x)M(y), \tag{4.5}$$
$$\det m = N!(-1)^{N_c}\bar B(y)B(x)\ \ \text{and}\ \ \det m^\dagger = N!\bar B(x)B(y), \tag{4.6}$$

to rewrite (4.3) in terms of the new fields[5]

$$z(x,y) = \sum_{k=0}^{N_c}\frac{(N_c-k)!}{N_c!k!}(\gamma^{2\delta_{\mu,0}}M(x)M(y))^k + \eta^\mu(x)\gamma^{N_c\delta_{\mu,0}}\mathrm{e}^{N_c\delta_{\mu,0}a_\tau\mu}\bar B(x)B(y)$$
$$+(-1)^{N_c}\eta^\mu(x)\gamma^{N_c\delta_{\mu,0}}\mathrm{e}^{-N_c\delta_{\mu,0}a_\tau\mu}\bar B(y)B(x),\ \ \mu\equiv(x,y)_\mu. \tag{4.7}$$

[5]For a more in-depth derivation of the combinatorial prefactors, see e.g. [12]. For a more elegant derivation using Weingarten functions, see [6].

Note that the series terminates after N_c terms due to the nilpotency of grassmann variables. Finally, we can utilize (4.7) to calculate the remaining integral in (4.2). We expand the exponential

$$\begin{aligned} Z_{SC} &= \int_\psi \prod_{x\in\Lambda} \mathrm{d}\psi(x)\mathrm{d}\bar{\psi}(x)\mathrm{e}^{2am_q\bar{\psi}(x)\psi(x)} \prod_{\mu=0}^{3} z(x, x+\hat{\mu}) \\ &= \int_\psi \prod_{x\in\Lambda} \mathrm{d}\psi(x)\mathrm{d}\bar{\psi}(x) \sum_{n_x=0}^{N_c} \frac{\left(2am_q\bar{\psi}(x)\psi(x)\right)^{n_x}}{n_x!} \prod_{\mu=0}^{3} z(x, x+\hat{\mu}) \end{aligned}$$

and notice the following local constraint coming from the nilpotency:

$$n_x + \sum_{\mu}^{3} k_{x,\mu} \stackrel{!}{=} N_c, \tag{4.8}$$

where $k_{x,\mu}$ is the exponent of the operator $M(x)M(x+\hat{\mu})$ in (4.7). Similarly, a non-zero contribution from the baryonic part of the one-link integral requires n_x and $k_{x,\mu}$ to vanish since the baryonic hoppings already consume all avialable color indices. By introducing a baryonic occupation number $l_{x,\mu}$ that locally fulfills

$$\sum_{\mu=0}^{3} l_{x,\mu} + l_{x,-\mu} = 0, \tag{4.9}$$

we can express Z_{SC} as a sum over occupation number configurations that satisfy (4.8) and (4.9):

$$Z_{SC} = \sum_{\{n_x,k_b,l\}} \prod_{b=(x,\mu)} \frac{(N_c-k_b)!}{N_c!k_b!}\gamma^{2k_b\delta_{\mu,0}} \prod_x \frac{N_c!}{n_x!}\left(2am_q\right))^{n_x} \prod_l \frac{\sigma(l)}{N_c!}\gamma^{N_cN_{0,l}}e^{N_\tau a_t\mu_B r_l}, \tag{4.10}$$

$$\text{with } \sigma(l) = (-1)^{r_l+N_-(l)+1} \prod_{(x,\mu)\in l} \eta^\mu(x).$$

Here, r_l denotes the winding number of baryonic loops in temporal direction, $N_{0,l}$ the total number of baryonic segments oriented in temporal direction and N_- the number negative baryonic segments.

To develop an intuition for the partition function above, we want to give a graphical representation of the three different types of occupation numbers. This graphical representation will also be relevant for analytical crosschecks later. The first term in Z_{SC} corresponds to mesonic hoppings $M(x)M(x+\hat{\mu})$, so-called dimers, with the occupation number $k_{x,\mu} \in \{0, 1, \ldots, N_c\}$. On the lattice, we depict them as unoriented lines connecting the sites x and $x+\hat{\mu}$:

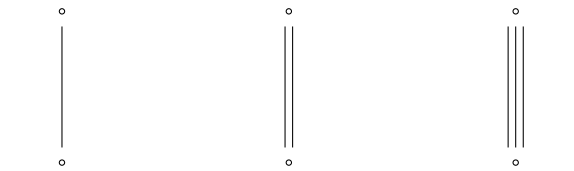

Figure 2: Graphical representation of mesonic hoppings $(M(x)M(x+\hat{\mu}))^{k_{x,\mu}}$.

The second term in Z_{SC} originates from the mass term $\mathrm{e}^{2am_q\bar{\psi}(x)\psi(x)}$ and is related to the occupation number $n_x \in \{0, 1, \ldots, N_c\}$. These objects are called monomers. We associate them with a number of dots at the site x:

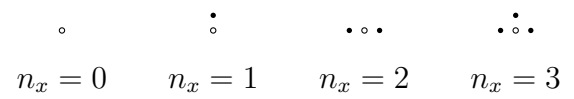

Figure 3: Graphical representation of mesonic variables $M(x)^{n_x}$.

The final term in Z_{SC} represents baryonic world lines with the occupation number $l_{x,\mu} \in \{-1, 0, 1\}$. We associate them with oriented lines:

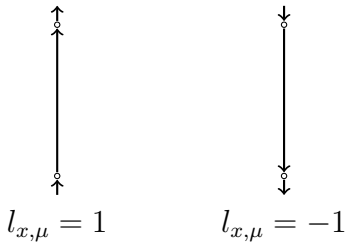

Figure 4: Graphical representation of baryonic hoppings $\bar{B}(x)B(x+\hat{\mu})$ and $\bar{B}(x+\hat{\mu})B(x)$.

In this graphical representation, the constraint (4.8) translates to the rule that at each lattice site - that is not part of a baryonic line - the number of monomers and dimers connected to that site is N_c. The second constraint (4.9) implies that the baryon segments form self-avoiding loops. According to (4.10), the sign of a configuration $\sigma(l)$ can be read off directly and only specific baryon configurations can create a negative sign. As seen in Fig. 40 in the appendix, these configurations only start to become important at high chemical potentials and low temperatures and are largely surpressed in the other regions of the μ, T-plane such that the sign problem is mostly mild.

5. Numerical methods

In this section, we gather the necessary computational methods to simulate the above system. We start by recalling the general Markov-Chain Monte-Carlo method. Afterwards, we describe the updating algorithm used to generate the occupation number configurations and finish with a description of the Jackknife sampling method for error estimation and the sign reweighting method.

5.1. Markov-Chain Monte-Carlo

For a reasonably sized four dimensional lattice, the number of configurations that contribute to Z_{SC} is so large that statistical methods are the only means to extract information from it. For that purpose, we will be using the Markov-Chain Monte-Carlo method. The ensemble average of an observable $\mathcal{O}$

$$\langle \mathcal{O} \rangle_e = \frac{\sum_{n,k,l} \mathcal{O}[n,k,l] W[n,k,l]}{\sum_{n,k,l} W[n,k,l]}$$

with $W[n,k,l]$ being the weightfactor of the configuration $C = [n,k,l]$ from (4.10), is approximated by the sample average

$$\langle \mathcal{O} \rangle_s = \frac{1}{N} \sum_{C_i} \mathcal{O}[n_i,k_i,l_i]$$

where the N configurations C_i follow the distribution induced by $W[n,k,l]$. This is called importance sampling. The configurations C_i are generated in a random sequence, the so-called Markov-Chain, where the probability to generate the configuration C_i depends only on the previous configuration C_{i-1}. The transition probabilities have to be normalized

$$\sum_i P(C_j|C_i) = 1, \tag{5.1}$$

and need to fulfill the ergodicity criterium

$$\exists n \in \mathbb{N} : \ (P^n)_{ij} > 0 \ \ \forall i,j$$

in order to ensure that the sequence of configurations can span the whole configuration space and is not limited to a certain subset of it. In order to achieve importance sampling, configurations generated from a given initial ensemble of configurations with distribution W_0 have to approach the equilibrium distribution $W[n,k,l]$ of (4.10)

$$\lim_{n\to\infty} P^n W_0 = W[n,k,l].$$

This implies that the equilibrium distribution $W[n,k,l]$ is a fixed point of the transition matrix P

$$P W_{\text{eq}} = W_{\text{eq}}, \tag{5.2}$$

which we require to be unique. This can be achieved if we require the detailed balance condition

$$P(C_i|C_j)W_{eq}(C_i) = P(C_j|C_i)W_{eq}(C_j) \tag{5.3}$$

to hold. Because then

$$\sum_{C_i} P(C_i|C_j)W_{eq}(C_i) = \sum_{C_i} P(C_j|C_i)W_{eq}(C_j) \overset{(5.1)}{=} W_{eq}(C_j).$$

5.2. Worm algorithm

In order to sample configurations in the dual representation, we make use of a class of cluster algorithms called worm algorithms that are well suited to update constrained systems like (4.10). Updating a configuration C_i to C_{i+1} happens in three distinct steps, a mesonic worm step, a baryonic worm step and a monomer update.

Monomer Update

We start with the simplest of the three: the monomer update. It is a local metropolis update that proposes to replace either a dimer with a pair of monomers at the two sites that are connected by the dimer or vice versa. At the start of this step, a random link is chosen with uniform probability. Another uniform random number decides whether the monomer number at the sites of this link should be increased or decreased. In the former case, the algorithm checks if the bond is occupied by a dimer. If not, the step ends and the configuration is not modified. If, however, the dimer occupation number is non-zero, a dimer on that link will be replaced by two monomers at the sites connecting that link if the acceptance check with probability

$$p_a = \frac{k_{x,\mu}(N_c + 1 - k_{x,\mu})}{(n_x + 1)(n_{x+\hat{\mu}} + 1)} \gamma^{-2\delta_{0,\mu}}$$

succeeds. In the latter case, it is checked if the monomer number on both sites is non-zero. If that is the case, the two monomers at the sites of the link are replace by a dimer with the probability

$$p_a = \frac{n_x n_{x+\hat{\mu}} \gamma^{2\delta_{0,\nu}}}{(k_{x,\mu} + 1)(N_c - k_{x,\mu})}.$$

A single update step can thus change the monomer number by ± 2 and 0. A small sketch to ilustrate the update is given in figure 5.

Figure 5: The local monomer update on the lattice.

Mesonic worm step

The mesonic worm step is based on the directed path algorithm which was first proposed in [5]. The step is seperated into two parts: active site updates and passive site updates. Active site updates delete a dimer while passive site updates create a dimer at a given link. The two steps are alternated until the mesonic worm stops.
The mesonic worm step starts by proposing a site that is not traversed by a baryon loop with uniform probability and continues to do so until a site is accepted. The probability for the acceptance test is

$$P = \frac{n_x}{N_c}.$$

Once a site is chosen, a quark source and sink are introduced to this site in the form of monomers. This first site defines the decomposition into active and passive sites. All sites that share the same parity with this first site are also called active. The introduction of the quark sources violates the Grassmann constraint (4.8) unless an adjacent dimer is deleted. Therefore, a direction $\hat{\mu}$ is proposed and accepted with the probability

$$P_\mu = \frac{k_{x,\hat{\mu}}}{N_c}.$$

The dimer on the chosen link is then deleted and the worm's head, that is one of the two initially introduced monomers, moves to the site $x+\hat{\mu}$. This site is now passive. Subsequently, a link for the addition of a dimer is chosen according to

$$P_{\hat{\nu}} = \frac{W_\nu}{\sum_\sigma W_\sigma}, \quad \text{with} \quad W_\sigma = \gamma^{2\delta_{0,\sigma}}.$$

By carrying the worm's head over to the new site $x + \hat{\mu} + \hat{\nu}$, we are again at an active site and have two possibilities: Either, there are monomers at this site and we can end the mesonic worm step by deleting a monomer with the probability

$$P_{\text{end}} = \frac{n_{x+\hat{\mu}+\hat{\nu}}}{N_c - k_{x+\hat{\mu},\hat{\nu}}},$$

or, we choose a new direction $\hat{\alpha} \neq \hat{\nu}$ with the probability

$$P_\alpha = \frac{k_{x+\hat{\mu}+\hat{\nu},\hat{\alpha}}}{N_c - k_{x+\hat{\mu},\hat{\nu}}}$$

and continue the update by deleting a dimer in this direction, moving the worm's tail to the new site and proceeding with the next passive site update. Note that in the chiral limit, the only two monomers on the lattice are the artificially introduced worm head and worm tail. Therefore, the update can only end when the worm head returns to its starting point. This leads to an increase in CPU-time per update step compared to the finite quark mass case. A sketch of a simple mesonic worm update is given in figure 6

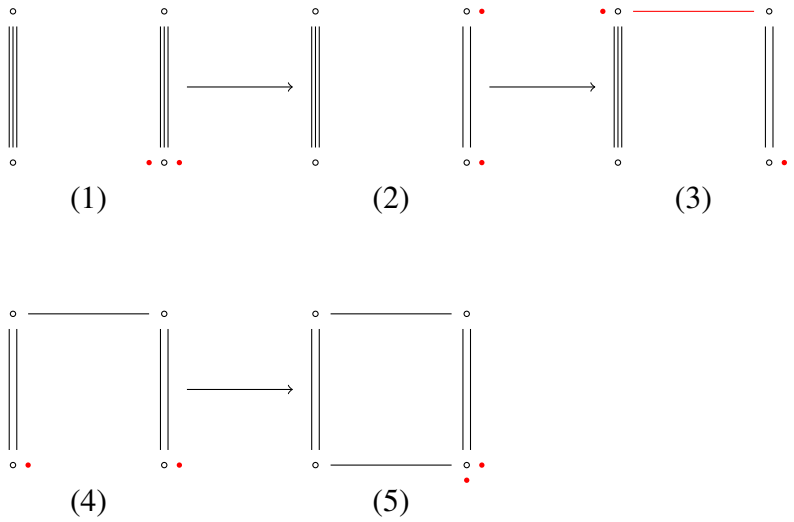

Figure 6: Exemplary mesonic worm step.

Baryonic worm step

Lastly, we want to discuss the baryonic worm step. Again, this step consists of active and passive site updates and we start by choosing with uniform probability a site that is either baryonic or touched by an N_c-dimer. In the latter case, we replace the N_c-dimer with a baryon segment $l_{x,\mu} = 1$, while in the former we proceed into the direction of negative baryon flux and delete this segment. At the passive site $x + \hat{\mu}$, we chose a new direction $\hat{\nu}$ with probability

$$P_\nu = \frac{W_{\hat{\nu}}}{\sum_\sigma W_\sigma} \quad \text{with } W_\sigma = \begin{cases} \gamma^{N_c \delta_{0,\sigma}} \mathrm{e}^{N_c a_\tau \mu (\delta_{\sigma,+0} - \delta_{\sigma,-0})} & \text{if } l_{x+\hat{\mu},\sigma} \neq 0 \vee k_{x+\hat{\mu},\sigma} = N_c \\ 0 \text{ else.} \end{cases}$$

and update the links according to $(l_{x+\hat{\mu},-\mu} \to l_{x+\hat{\mu},-\mu} - 1, k_{x+\hat{\mu},-\mu} = 0, l_{x+\hat{\mu},\nu} \to l_{x+\hat{\mu},\nu} + 1)$ if $l_{x+\hat{\mu},\nu} \neq 0$ and $k_{x+\hat{\mu},\nu} = N_c$ in the other case. Site $x + \hat{\mu} + \hat{\nu}$ is active again and we face three options to proceed. If the site happens to be the starting point of the worm evolution, the update ends. Otherwise, if the site is touched by an N_c-dimer, we proceed in this direction by replacing it with a baryon as above. If the site is traversed by a baryon, we continue into the direction of negative baryon flux and delete this segment. Afterwards, we continue with the passive site update as before.

5.3. Error estimates

The configurations generated with the above algorithm are auto-correlated such that the empirical mean and variance are not reliable estimates of the ensemble mean and variance. Instead, we will use the Jackknife method to obain reliable error estimates. Given a set of N measurements of the observable $\mathcal{O}$, we devide the dataset into m subsets of size $M < N$. Then, new data sets N_i are constructed by removing the i'th block from the original set. We calculate the

empirical mean of $\mathcal{O}$ on these reduced data sets:

$$\tilde{\mathcal{O}}_i = \frac{1}{M}\sum_{k=1}^{M}\mathcal{O}_k$$

and then form the mean of those means

$$\tilde{\mathcal{O}} = \frac{1}{m}\sum_{l=1}^{m}\tilde{\mathcal{O}}_l.$$

We can use this new mean to calculate the bias B

$$B = (m-1)(\tilde{\mathcal{O}} - \hat{\mathcal{O}}),$$

where $\hat{\mathcal{O}}$ denotes the empirical mean. Correcting for this bias results in the Jackknife estimator $\hat{J}$

$$\hat{J} = \hat{\mathcal{O}} - B = \frac{1}{m}\sum_{l=1}^{m}\hat{J}_l, \tag{5.4}$$

with the new Jackknife pseudo-values J_i

$$J_i = m\hat{\mathcal{O}} - (m-1)\tilde{\mathcal{O}}. \tag{5.5}$$

These are used to form the new variance estimator σ_J via

$$\sigma_j = \frac{1}{m(m-1)}\sum_{i=1}^{m}(\hat{J}_i - \hat{J})^2 \tag{5.6}$$

$$= \frac{m-1}{m}\sum_{i=1}^{m}(\tilde{\mathcal{O}}_i - \tilde{\mathcal{O}})^2. \tag{5.7}$$

5.4. Sign reweighting

The dual formulation of strong coupling QCD still faces a mild sign problem that has to be addressed. For that purpose, we make use of the sign reweighting strategy. That is, we interpret the sign of a configuration as an additional observable and measure an observable $\mathcal{O}$ by

$$\langle\mathcal{O}\rangle = \frac{\langle\sigma\mathcal{O}\rangle}{\langle\sigma\rangle}. \tag{5.8}$$

Writing $\langle\sigma\rangle = \exp(-V_4\Delta f)$, where Δf is the difference between the real and the sign-quenched free energy density, we see that the average sign decreases exponentially with the volume. If $\langle\sigma\rangle$ becomes small, e.g. on large lattices, the cancellations between numerator and denominator lead to severe numerical errors. In fact, one can show that the sign-problem is NP-hard [13].

6. Equation of State in the T, μ-plane

6.1. Observables

The goal of this section is to determine the representation of physical observables like the energy density or the pressure in terms of the dual variables discussed in previous sections. These representations are obtained by taking derivatives of the thermodynamic potential Φ, naturally related to the partition function Z_{SC} by

$$\Phi(T, \mu, V) = -T \log Z.$$

At the same time, Φ is obtained from the energy E by Legendré transformation

$$\Phi(T, V, \mu) = E - TS - \mu N$$

which together with $\mathrm{d}E = T\mathrm{d}S - p\mathrm{d}V + \mu\mathrm{d}N$ gives

$$\mathrm{d}\Phi = -p\mathrm{d}V - S\mathrm{d}T - N\mathrm{d}\mu$$

such that the following thermodynamic relations hold:

$$\left(\frac{\partial\Phi}{\partial V}\right)_{\mu,T} = -p, \quad \left(\frac{\partial\Phi}{\partial T}\right)_{V,\mu} = -S, \quad \left(\frac{\partial\Phi}{\partial \mu}\right)_{T,V} = -N.$$

The combination of these relations with the partition function (4.10) identifies the observables that we need to calculate in Monte-Carlo simulations. We begin by expressing the baryon number density $n_B = \frac{N_B}{V}$ in terms of the dual variables:

$$\begin{aligned} n_B = \frac{N_B}{V} &= \frac{T}{V}\left(\frac{\partial \log Z}{\partial \mu_B}\right)_{T,V} = \frac{1}{a_\tau N_\tau a^3 N_\sigma^3}\left(\frac{\partial \log Z}{\partial \mu_B}\right)_{a_\tau, a} \\ &= \frac{1}{a_\tau N_\tau a^3 N_\sigma^3}\frac{1}{Z}\sum_{\{n,k,l\}} \cdots \frac{\partial}{\partial \mu_B}\frac{\sigma(l)}{N_c!}\gamma^{N_c N_{0,l}} e^{N_\tau a_t \mu_B r_l} \\ &= \frac{1}{a_\tau N_\tau a^3 N_\sigma^3}\frac{1}{Z}\sum_{\{n,k,l\}} \cdots a_\tau N_\tau r_l \frac{\sigma(l)}{N_c!}\gamma^{N_c N_{0,l}} e^{N_\tau a_t \mu_B r_l} \\ &= \frac{\langle r_l \rangle}{a^3 N_\sigma^3}, \end{aligned} \tag{6.1}$$

and find that the baryon density corresponds to the average winding number of the baryonic world lines in temporal direction. This can be used in conjunction with the definition of the partition sum $Z = \mathrm{Tr}\ \mathrm{e}^{-\beta(H-\mu N)}$ to obtain the energy density $\epsilon = \frac{E}{V}$ through the relation

$$\frac{1}{V}\frac{\partial \log Z}{\partial \beta} = -\epsilon + \mu_B n_B. \tag{6.2}$$

On the left-hand side, we apply the definition of the temperature (3.14) to cast the β-derivative in terms of derivatives with respect to the temporal lattice spacing a_τ:

$$\frac{\partial \log Z}{\partial \beta} = \frac{\partial \log Z}{\partial (a_\tau N_\tau)} = \frac{1}{N_\tau}\frac{1}{Z}\frac{\partial Z}{\partial a_\tau} = \frac{1}{N_\tau}\frac{1}{Z}\left(\frac{\partial \xi}{\partial a_\tau}\frac{\partial \gamma}{\partial \xi}\frac{\partial Z}{\partial \gamma} + \left.\frac{\partial Z}{\partial a_\tau}\right|_\gamma\right).$$

The second term is again proportional to the winding number $\langle r_l \rangle$ such that we obtain

$$\frac{1}{V}\frac{\partial \log Z}{\partial \beta} = \frac{1}{VN_\tau}\frac{1}{Z}\frac{\partial \xi}{\partial a_\tau}\frac{\partial \gamma}{\partial \xi}\frac{\partial Z}{\partial \gamma} + \mu_B \frac{\langle r_l \rangle}{V}.$$

By comparing to (6.2), we see that the winding number term is canceled and we obtain a formula for the energy density

$$\begin{aligned}
\epsilon &= -\frac{1}{VN_\tau}\frac{1}{Z}\frac{\partial \xi}{\partial a_\tau}\frac{\partial \gamma}{\partial \xi}\frac{Z}{\gamma} = \frac{\xi}{a_\tau N_\tau a^3 N_\sigma^3}\frac{\partial \gamma}{\partial \xi}\frac{1}{Z}\frac{\partial Z}{\partial \gamma} \\
&= \frac{\xi}{a_\tau N_\tau a^3 N_\sigma^3}\frac{\partial \gamma}{\partial \xi}\frac{1}{Z}\sum_{\{n,k,l\}} \cdots \frac{\partial}{\partial \gamma}\gamma^{2N_{D_t}+N_c N_{B_t}} \cdots \\
&= \frac{\xi}{a_\tau N_\tau a^3 N_\sigma^3}\frac{\partial \gamma}{\partial \xi}\frac{1}{Z}\sum_{\{n,k,l\}} \cdots (2N_{D_t} + N_c N_{B_t})\,\gamma^{2N_{D_t}+N_c N_{B_t}-1} \cdots \\
&= \frac{1}{a_\tau N_\tau a^3 N_\sigma^3}\frac{\xi}{\gamma}\frac{\partial \gamma}{\partial \xi}\langle 2N_{D_t} + N_c N_{B_t}\rangle. \qquad (6.3)
\end{aligned}$$

We used $\frac{\partial \xi}{\partial a_\tau} = -\frac{\xi}{a_\tau}$ in the first line and introduced in the second line the new quantities N_{D_t} and N_{B_t} which are the total number of temporal dimers and temporal baryon segments, respectively. The energy density comes with a peculiarity not shared by most other observables in strong coupling lattice QCD: it depends not only on the physical anisotropy ξ but also on its derivative with respect to the bare coupling γ, i.e. it depends on the "running" of the anisotropy coupling. The exact determination of $\xi(\gamma)$ is therefore an important prerequisite for the study of the Equation of State and related quantities.
In a similar manner, we can calculate the pressure by relating the volume derivative to derivatives w.r.t. the spatial lattice spacing a:

$$\begin{aligned}
p &= -\frac{\partial \Phi}{\partial V} = T\frac{\partial \log Z}{\partial V} = \frac{1}{a_\tau N_\tau}\frac{\partial \log Z}{\partial (a^3 N_\sigma^3)} = \frac{1}{a_\tau N_\tau 3a^2 N_\sigma^3}\frac{\partial \log Z}{\partial a} \\
&= \frac{1}{a_\tau N_\tau 3a^2 N_\sigma^3}\frac{1}{Z}\left(\frac{\partial \xi}{\partial a}\frac{\partial \gamma}{\partial \xi}\frac{\partial Z}{\partial \gamma} + \left.\frac{\partial Z}{\partial a}\right|_\gamma\right).
\end{aligned}$$

Evaluating the first term of this expression yields, again, the expectation value of the temporal dimer and baryon segments.

The second term is related to the total number of monomers N_m:

$$\begin{aligned} p &= \frac{1}{a_\tau N_\tau 3a^2 N_\sigma^3}\left(\frac{\xi}{a}\frac{\partial\gamma}{\partial\xi}\frac{1}{\gamma}\left\langle 2N_{D_t}+N_cN_{B_t}\right\rangle + \frac{1}{Z}\left.\frac{\partial Z}{\partial a}\right|_\gamma\right) \\ &= \frac{1}{a_\tau N_\tau 3a^2 N_\sigma^3}\left(\frac{\xi}{a}\frac{\partial\gamma}{\partial\xi}\frac{1}{\gamma}\left\langle 2N_{D_t}+N_cN_{B_t}\right\rangle + \frac{1}{Z}\sum_{\{n,k,l\}}\cdots\frac{\partial}{\partial a}\left(2am_q\right)^{N_m}\cdots\right) \\ &= \frac{1}{a_\tau N_\tau 3a^2 N_\sigma^3}\left(\frac{\xi}{a}\frac{\partial\gamma}{\partial\xi}\frac{1}{\gamma}\left\langle 2N_{D_t}+N_cN_{B_t}\right\rangle + \frac{1}{Z}\sum_{\{n,k,l\}}\cdots N_m 2m_q\left(2am_q\right)^{N_m-1}\cdots\right) \\ &= \frac{1}{3a_\tau N_\tau a^3 N_\sigma^3}\left(\frac{\xi}{\gamma}\frac{\partial\gamma}{\partial\xi}\left\langle 2N_{D_t}+N_cN_{B_t}\right\rangle + \left\langle N_m\right\rangle\right). \end{aligned} \tag{6.4}$$

In combination with the result for the energy density we see that the interaction energy $\epsilon - 3p$ in the strong coupling limit is given by

$$\epsilon - 3p = \frac{-\langle N_m\rangle}{a_\tau N_\tau a^3 N^3}. \tag{6.5}$$

In the massless case, where the monomer density is always zero we even have

$$\epsilon - 3p = 0, \tag{6.6}$$

which is the equation of state for non-interacting, massless, relativistic particles. These results reflect the lattice version of (2.5)[6]. An anomalous contribution as in (2.9) is absent in the strong coupling limit.
For now, we want to conclude the discussion of the observables in the dual representation by calculating the operator for the chiral condensate $\bar\psi\psi$. It is defined as

$$\langle\bar\psi\psi\rangle = \frac{T}{V}\frac{\partial\log Z}{\partial m_q}, \tag{6.7}$$

and couples to the monomer density

$$\begin{aligned} \langle\bar\psi\psi\rangle &= \frac{1}{a_\tau N_\tau a^3 N_\sigma^3}\frac{1}{Z}\sum_{\{n,k,l\}}\cdots\frac{\partial}{\partial m_q}\left(2am_q\right)^{N_m}\cdots \\ &= \frac{1}{a_\tau N_\tau a^3 N_\sigma^3}\frac{1}{Z}\sum_{\{n,k,l\}}\cdots 2aN_m\left(2am_q\right)^{N_m-1}\cdots \\ &= \frac{\langle N_m\rangle}{m_q a_\tau N_\tau a^3 N_\sigma^3} = \frac{\langle n_m\rangle}{m_q a_\tau a^3}. \end{aligned} \tag{6.8}$$

The relations are summarized in tab. 1.

[6]Recall: $\Theta^\mu_\mu = \epsilon - 3p$.

Physical observable	Rep. in dual variables
$a^4\epsilon$	$\frac{\xi^2}{\gamma}\frac{\partial\gamma}{\partial\xi}\langle 2n_{D_t} + N_c n_{B_t}\rangle$
$a^4 p$	$\frac{\xi}{3}\left(\frac{\xi}{\gamma}\frac{\partial\gamma}{\partial\xi}\langle 2n_{D_t} + N_c n_{B_t}\rangle + \langle n_M\rangle\right)$
$a^4\langle\bar{\psi}\psi\rangle$	$\frac{\xi}{m_q}\langle n_m\rangle$
$a^3 n_B$	$\frac{\langle r_l\rangle}{N_\sigma^3} = \langle\omega_l\rangle$

Table 1: Summary of the phyiscal observables expressed in terms of the occupation number representation of strong coupling lattice QCD.

6.2. Anisotropy calibration

In the previous section, we found that the anisotropy not only enters in the setting of the temperature but also plays a central role in determining even the most basic thermodynamical quantities. Therefore a precise, non-perturbative method to calculate $\xi(\gamma)$ is needed. For that purpose we adopt a method initially developed in [9] and [14] that relies on comparing fluctuations of conserved currents in spatial and temporal direction to determine the physical anisotropy.
We begin by recalling the Grassmann constraint (4.8) and the baryonic constraint (4.9). These two can be united into the constraint

$$n_x + \sum_{\pm\mu}\left(k_{x,\mu} + \frac{N_c}{2}|l_{x,\mu}|\right) \stackrel{!}{=} N_c. \tag{6.9}$$

We can rearrange the expression

$$\sum_{\pm\mu}\left(k_{x,\mu} + \frac{N_c}{2}|l_{x,\mu}| - \frac{N_c}{2d}\right) = -n_x,$$

and define the current $j_\mu(x)$ as the summand of the left hand side multiplied with the parity $\sigma_x = \pm 1$ of the site x:

$$j_\mu(x) = \sigma_x\left(k_{x,\mu} + \frac{N_c}{2}|l_{x,\mu}| - \frac{N_c}{2d}\right).$$

This current then fulfills the discrete local Gauss' law

$$\sum_{\mu=0}^{d}\left(j_\mu(x) - j_\mu(x-\hat{\mu})\right) = -\sigma_x n_x. \tag{6.10}$$

We define conserved charges Q_μ by summing $j_\mu(x)$ over all lattice sites in directions perpendicular to μ

$$Q_\mu = \sum_{\{(x,\nu)\ |\ \nu\perp\mu\}} j_\nu(x). \tag{6.11}$$

The fluctuations $(\Delta Q_\mu)^2 = \langle Q_\mu^2 \rangle - \langle Q_\mu \rangle^2$ of these charges should coincide if the lattice is hypercubic, i.e. if $a = a_\tau$. As the spatial lattice is isotropic, the d spatial charge fluctuations are conveniently combined into the observable[7]

$$Q_s^2 = \frac{1}{d} \sum_{i=1}^{d} Q_i^2 \tag{6.12}$$

while $Q_t^2 = Q_0^2$. For fixed temporal and spatial lattice extends N_t and N_s and varying values of the anisotropy coupling γ, the two averages $\langle Q_s^2 \rangle$ and $\langle Q_t^2 \rangle$ are computed and the point at which

$$\langle Q_s^2 \rangle(\gamma) \stackrel{!}{=} \langle Q_t^2 \rangle(\gamma) \tag{6.13}$$

determines γ_{np} such that $\xi(\gamma_{\mathrm{np}}) = \frac{N_t}{N_s}$. This process is repeated for various values of $\frac{N_t}{N_s}$. The result is fitted with a suitable Ansatz to obtain an analytic expression for $\xi(\gamma)$ from which the derivative $\frac{\partial \xi(\gamma)}{\partial \gamma}$ can be estimated.

A few notes on technical details are in order. The calculations were performed[8] on lattices with $N_\sigma = 10$ and $N_\tau = \xi N_\sigma$. Evidently, calibrating $\xi(\gamma)$ for large ξ becomes increasingly difficult on lattices with large N_σ. However, it was shown in [9] that the convergence to the thermodynamic limit is very quick, such that calculations on $N_s = 10$ lattice suffice for our purposes. Furthermore, the following approximation is used: Instead of simulating the full $SU(3)$-theory with baryons, it suffices to use the gauge group $U(3)$ in which baryons are absent. This is justified since the calibration is performed at small temperatures and at $\mu_B = 0$ where baryons are strongly surpressed and contribute only insignificantly to the above charges. The data is fitted with the ansatz

$$\begin{aligned}
\frac{\xi}{\gamma^2}(x, am_q) &= \frac{a(x)}{1 + b(x)(am_q) + c(x)\sqrt{am_q}}, \quad \text{where } x = \frac{1}{\xi^2} \text{ and} \\
a(x) &= A_0 \left(\left(1 + A_1 x + A_2 x^2 + A_3 x^3\right) - (1 + A_1 + A_2) \right) + 1 \\
b(x) &= B_0 \left(\frac{1 + B_1 x + B_2 x^2}{1 + B_3 x + B_4 x^2} - \frac{1 + B_1 + B_2}{1 + B_3 + B_4} \right) \\
c(x) &= C_0 \left(\frac{1 + C_1 x + C_2 x^2}{1 + C_3 x + C_4 x^2} - \frac{1 + C_1 + C_2}{1 + C_3 + C_4} \right).
\end{aligned} \tag{6.14}$$

Index	A	B	C
0	0.7795	2.1103	-0.7098
1	0.2310	74.7155	2.2442
2	0.0554	-28.2623	0.2313
3	$4.7621 \cdot 10^{-7}$	229.6297	2.1162
4	-	908.1057	0.1946

Table 2: Fit-parameters for (6.14).

[7] $\langle Q_\mu \rangle = 0$ in the chiral limit.

[8] The simulations and data analysis for the anisotropy calibration were performed by Dr. Wolfgang Unger.

The result of the anisotropy calibration for various quark masses is presented in Fig. 7 and the fit parameters are given in Tab. 2. The derivative $\frac{\partial\gamma}{\partial\xi}$ which contributes to the pressure and the energy density is shown in Fig. 8.

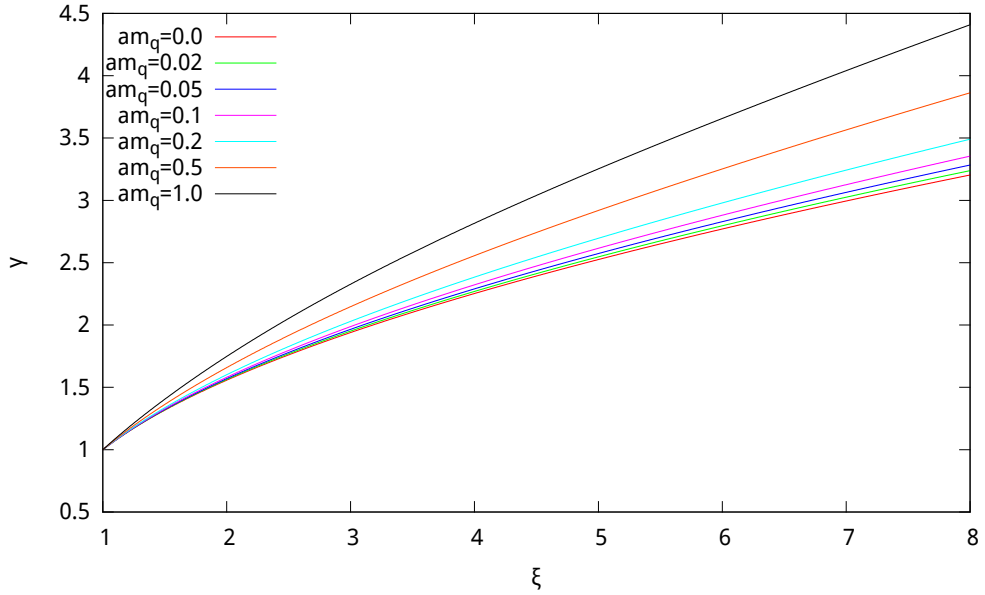

Figure 7: Calibrated anisotropy coupling γ as a function of ξ for different quark masses.

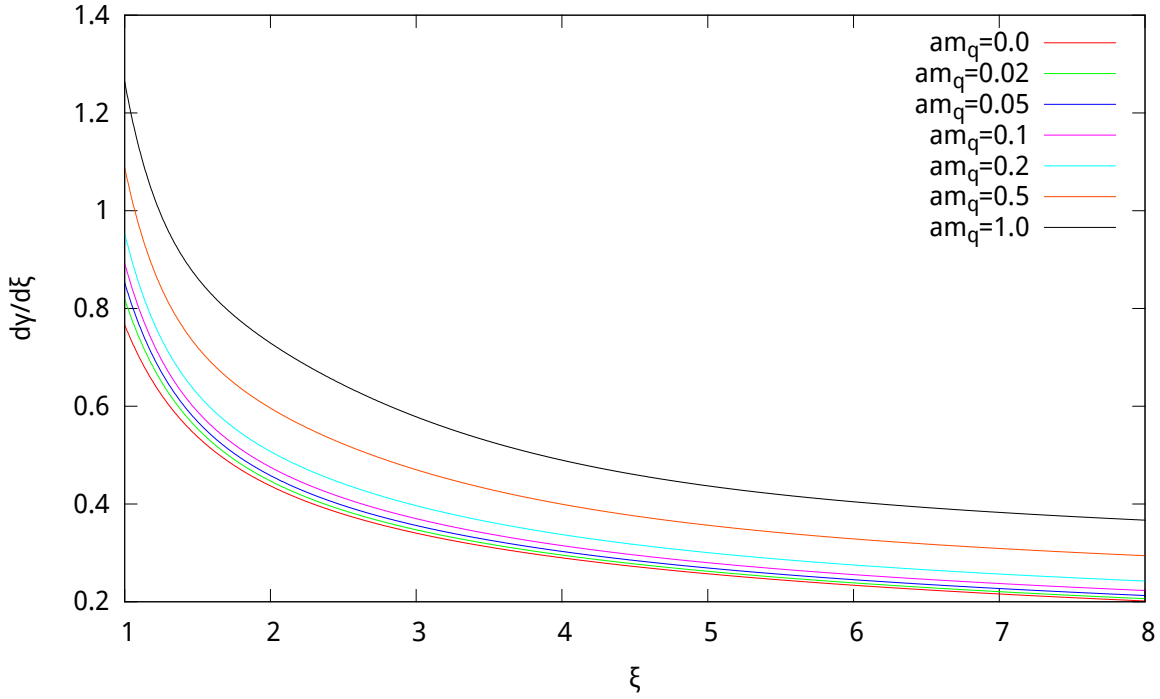

Figure 8: The derivative $\frac{\partial\gamma}{\partial\xi}$ plotted versus ξ for different quarks masses.

6.3. Results

With the identification of the relevant operators in section 6.1 and the calibration of the anisotropy in the previous section, we are now in the position to begin the calculation of thermodynamic observables of strong coupling lattice QCD. As an introductory step, we want to start by calculating the energy density of $U(3)$ and $SU(3)$ theories at $\mu = 0$ and $m_q = 0$. From there, we investigate the effect of introducing a chemical potential and a non-zero quark mass. Finally, we compute the energy density, pressure and baryon density across the full μ,T-plane.

6.3.1. Energy density of massless quarks at $\mu = 0$

The dual representation of one flavor of massless staggered fermions with gauge group $U(3)$ in the strong coupling limit is particularly simple because baryons and monomers are not present and the only degrees of freedom on the lattice are the dimers. Such a pure dimer system is expected to behave like a gas of free mesons in many aspects. An example for this was already given in (6.6), the dimer system fulfills the equation of state of a gas of free relativistic particles. Introducing baryons to the system by changing the gauge group to $SU(3)$ can potentially change such a behaviour as excluded volume effects between baryons induce a nuclear potential in strong coupling QCD [12]. In terms of the energy density, we therefore expect a behavior similar to the Stefan-Boltzmann law $\epsilon = \frac{\pi^2}{30} T^4$ for the $U(3)$-case and deviations from that for $SU(3)$.
To measure the energy, we sample the temporal dimer and baryon-segment density on lattices with $N_\sigma = 16$ and $N_\tau = \{4, 6, 8, 10, 12\}$. The temperature is varied by picking 6 values of γ that correspond to $\xi = \{1, 2, 3, 4, 5, 6\}$. This allows us to have the temperatures ranging from $aT_{\min} = \frac{1}{12}$ to $aT_{\max} = \frac{6}{4}$. We also subtract the $T = 0$ contribution

$$a^4 \epsilon_0 = \lim_{N_\sigma \to \infty} \frac{\xi^2}{\gamma} \frac{\partial \gamma}{\partial \xi} \langle 2n_{D_t} + 3n_{B_t} \rangle \Big|_{N_\tau = \xi N_\sigma} \tag{6.15}$$

which we estimate by computing $a^4 \epsilon_0(\xi)$ for different N_σ followed by an extrapolation towards $N_\sigma \to \infty$, see e.g. Fig. 9a.

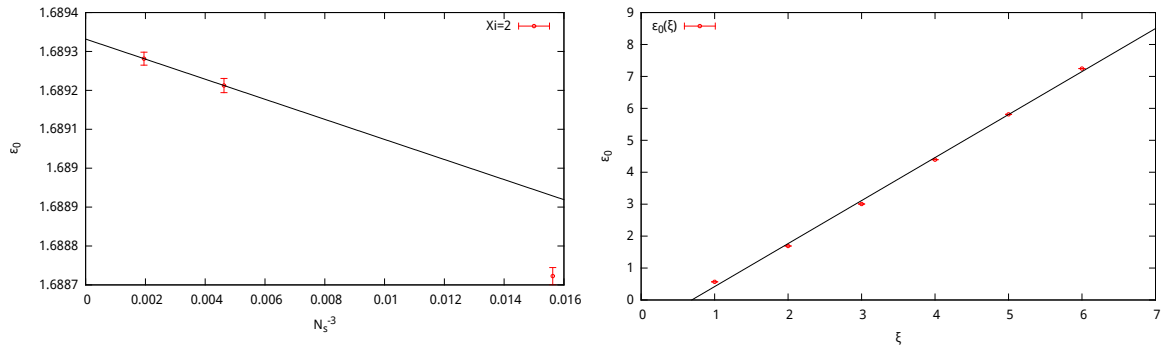

(a) **(b)**

Figure 9: Left: Exemplary extrapolation of $\epsilon_0(\xi)$. Right: Vacuum contribution ϵ_0 versus ξ.

The results for the energy density in $U(3)$ and $SU(3)$ theory are shown in Fig. 10 and Fig. 11. The $U(3)$-Data matches the Stefan-Boltzmann law very precisely especially at low and high temperatures but exhibits slight deviations from it at intermediate temperatures of $\left(\frac{T}{T_c}\right)^4 \sim 0.01$. The inclusion of baryons with the change to $SU(3)$ results in deviations especially at higher temperatures. The energy density starts to form a plateau above T_c and the slope differs significantly from the Stefan-Boltzmann factor $\frac{\pi^2}{30}$.

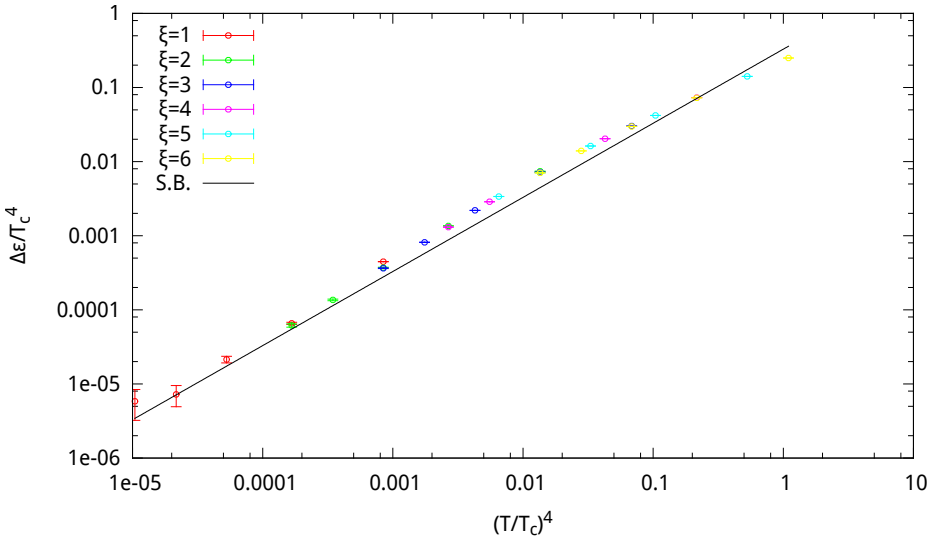

Figure 10: The energy density for the $U(3)$ theory at $\mu = 0$.

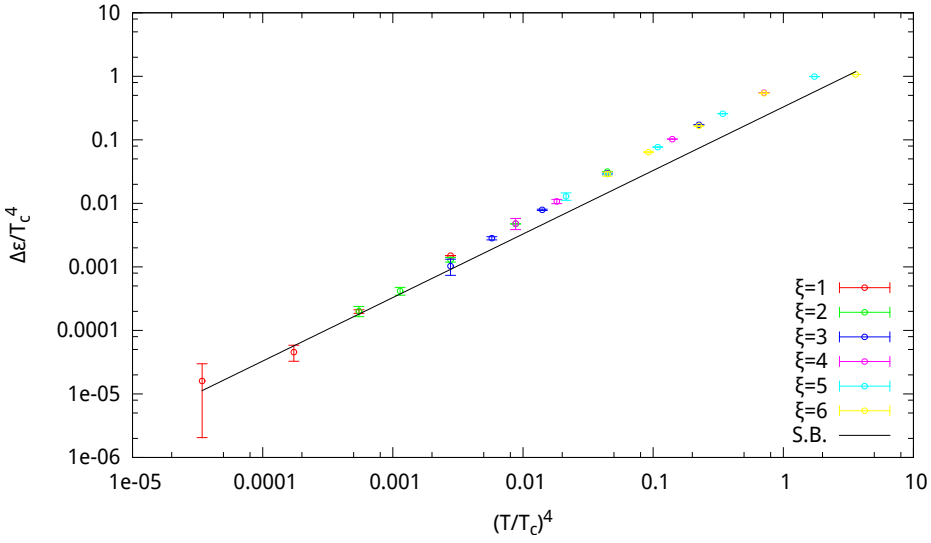

Figure 11: The energy density for the $SU(3)$ theory at $\mu = 0$.

6.3.2. The effect of finite quark mass

Taking the above results as a basis, we have multiple directions to explore in parameter space. We first start by including a finite quark mass to the calculations at $\mu = 0$. This introduces monomers as new degrees of freedom to our system. These do not contribute directly to the energy density (6.3) but reduce the possible sites that dimers can be attached to. Therefore we expect that the increase of quark mass will yield a gradual decrease in energy density. Additionally, the pressure now obtains a contribution from the monomer density such that $\epsilon - 3p \neq 0$.
Motivated by the experience gained when performing the above $m_q = 0$, $\mu = 0$ simulations, we also implement modifications to the simulation strategy. While the combination of lattices with different N_τ allows us to reach very low temperatures, the numerical effort neccesary to perform these simulations grows dramatically. The physically interesting region is, however, around the critical temperature $T_c = 1.089$ [14] which is easily reached by the $N_\tau = 4$ simulations. Furthermore, we noticed that extrapolating ϵ_0 towards the infinite volume limit has only a very small effect and we are already quite close to the infinite volume limit with simulations on $10^3 \times \xi \cdot 10$ lattices. Therefore, the following simulations are all performed on $10^3 \times 4$ lattices and vacuum contributions are approximated by calculations on $10^3 \times \xi \cdot 10$ lattices. The chosen temperatures range from $aT = 0.4$ to $aT = 2$ by choosing γ according to (6.14) such that $\xi = \{1.6, 2.0, 2.6, \ldots, 8\}$. The results for energy density, pressure and interaction energy are depicted in Fig. 12, Fig. 13 and Fig. 14, respectively.

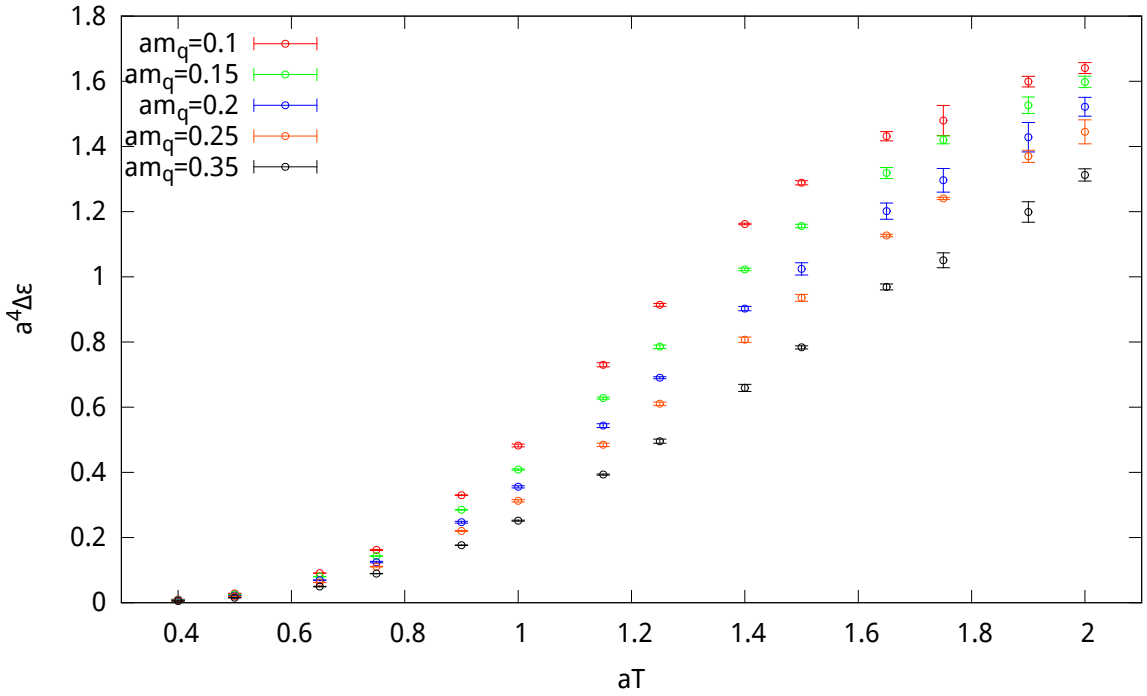

Figure 12: Energy density as a function of the temperature at $\mu = 0$ for different quark masses.

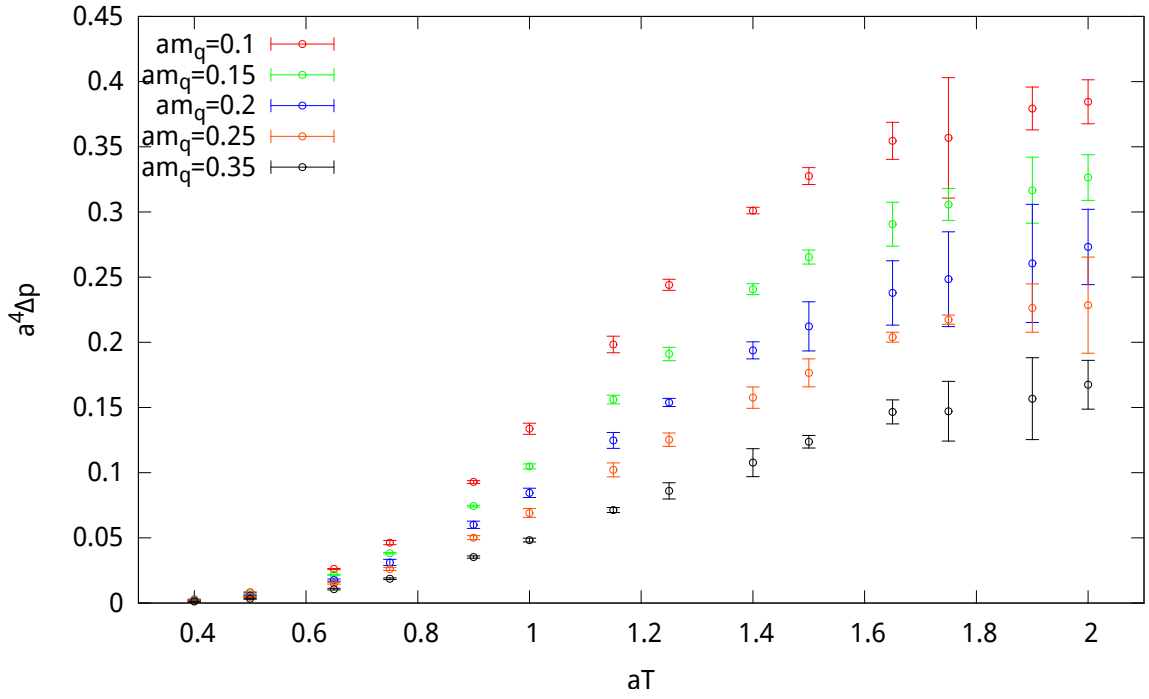

Figure 13: Pressure versus temperature for different quark masses.

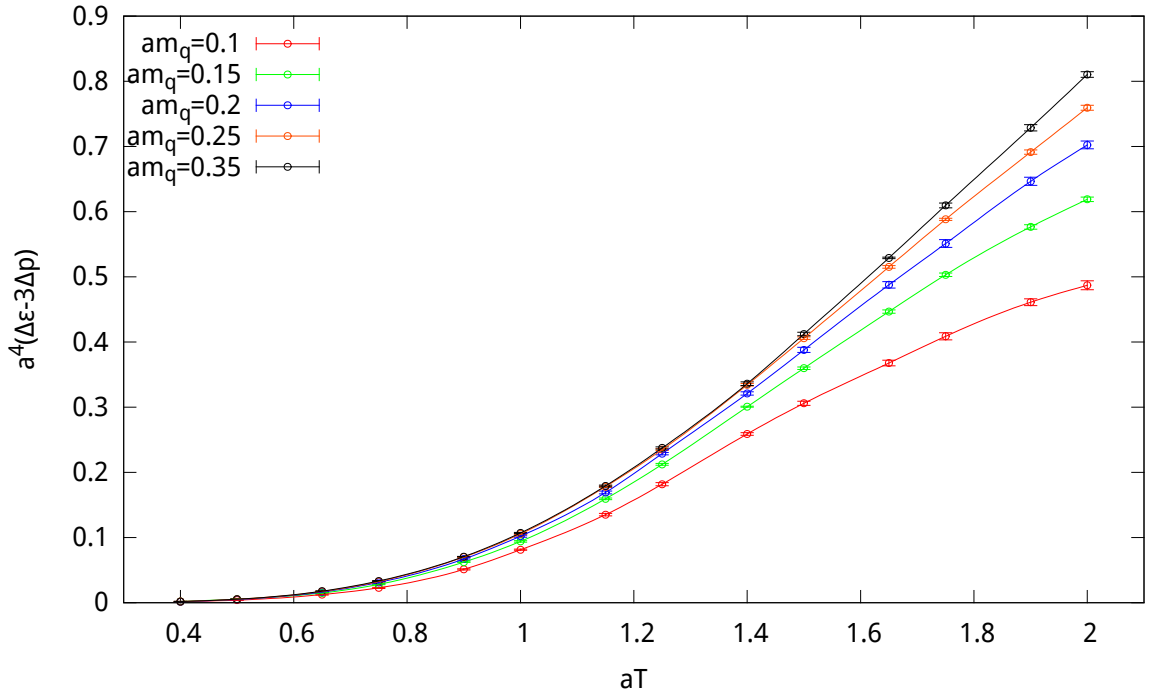

Figure 14: Interaction energy vs. temperature for different quark masses.

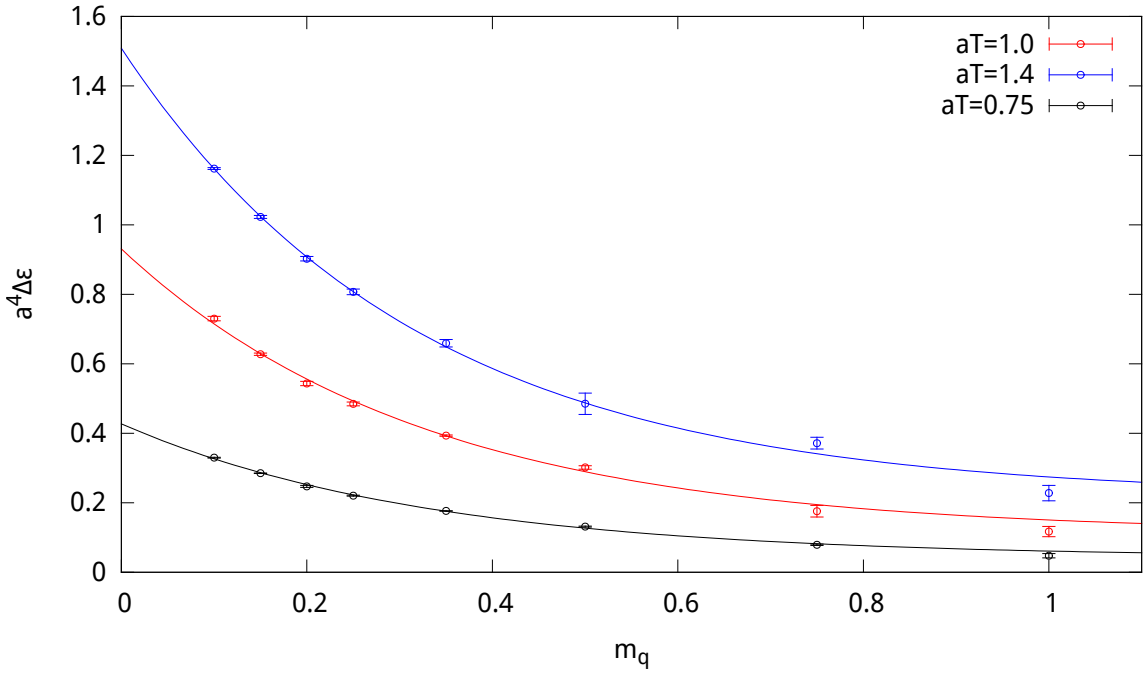

Figure 15: Quark mass dependence of the energy density for selected temperatures.

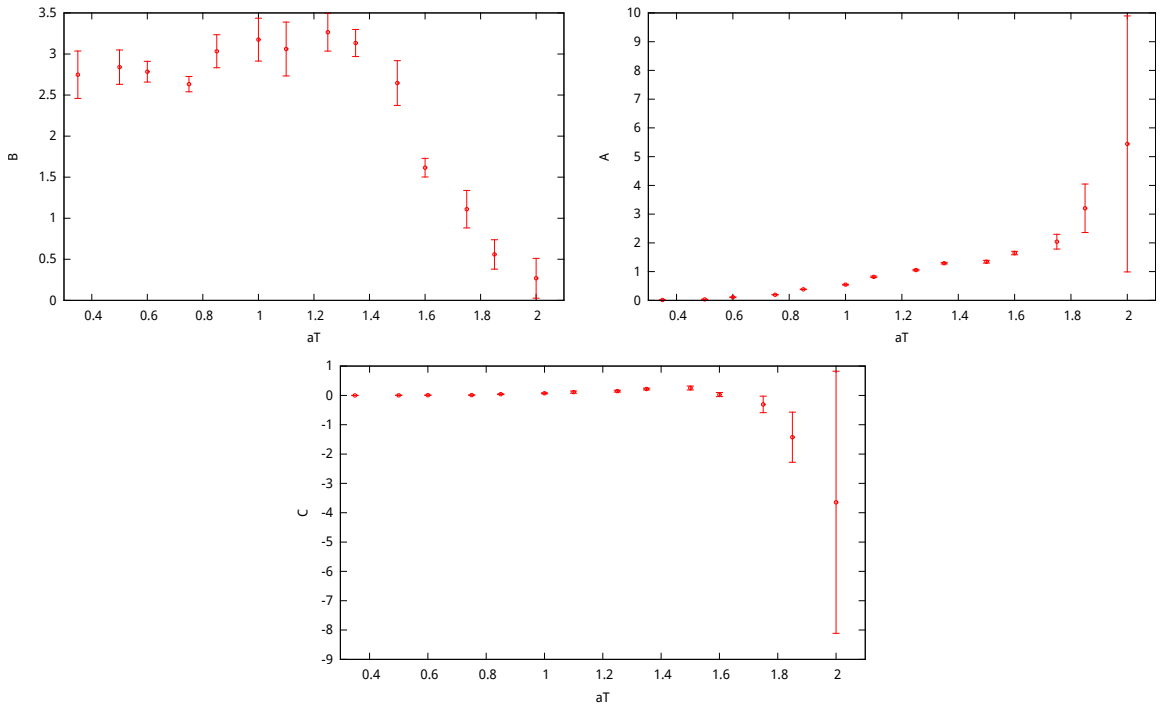

Figure 16: Temperature dependence of the fit-parameters B (left), A (right), C (bottom).

Indeed, we find that a finite quark mass suppresses the energy density. Furthermore, the plateau that formed at high temperatures in the massless case shifts with increasing quark mass further to higher temperatures. While a decrease of the slope of ϵ is visible at $m_q = 0.1$ at high temperatures, the energy density at $am_q = 0.5$ grows approximately linear from $aT = 1$ onwards. For the pressure, we find a similar shape with a slightly more pronounced bend towards higher temperatures that remains visible even for $am_q = 0.5$. The interaction energy $\epsilon - 3p$, on the other hand, increases with the quark mass since it is directly proportional to the monomer density $\langle n_M \rangle$. We can quantify these findings further. The quark mass dependence of the energy density for three selected temperatures is shown in Fig. 15. We fit the data with a simple exponential ansatz

$$a^4 \Delta\epsilon(am_q)|_{aT} = A \exp(-B \cdot am_q) + C$$

and find that increasing the quark mass leads to an exponential suppression of the energy density for a large range of temperatures which gradually flattens to a linear suppresion for the largest temperatures. This is also represented in the temperature dependence of the fit-parameters in Fig. 16. The exponential suppression factor B remains constant up to $aT \sim 1.3$ and drops significantly from there on. The amplitude A grows linearly up to $aT \sim 1.7$ and abruptly increases for the last two temperatures. The shift C remains close to $C = 0$ for all but the highest three temperatures.

6.3.3. Including the baryon chemical potential

Finally, we want to include the baryon chemical potential into our simulations. This will result in a favoring of baryon hoppings in temporal direction over anti-baryon hoppings. Hence, the average density of temporal baryon segments $\langle \omega_l \rangle$ will increase such that a positive net-baryon density n_B forms. In principle, we have to repeat the anisotropy calibration for each value of the chemical potential that we want to use for simulations. At zero temperature, where the anisotropy calibration is performed, the silver blaze property is expected to hold. That is, the physics at zero temperature is independent of μ_B for chemical potentials smaller than μ_c. As already mentioned, baryons are strongly suppressed at $(T, \mu) = (0, 0)$ and do not contribute significantly to the charges needed to determine $\xi(\gamma)$. Due to the silver-blaze property, we expect this to be true for $\mu < \mu_c$ as well. Therefore, we uphold our approximation to calculate $\xi(\gamma)$ only for $U(3)$ and use the same $\xi(\gamma)$ from (6.14) for the $\mu \neq 0$ simulations. We keep the same lattice sizes and temperatures as before but restrict our simulations to two different quark masses $am_q = 0.1$ and $am_q = 0.05$ as the number of simulations that need to be performed to yield an accurate scan of the μ, T-plane is rather large. In μ_B-direction, we choose a stepsize between $\Delta\mu_B = 0.3$ at small chemical potentials to $\Delta\mu_B = 0.03$ around the first order transition at higher chemical potentials. For a better visualization, we interpolate the result with thin plate splines.

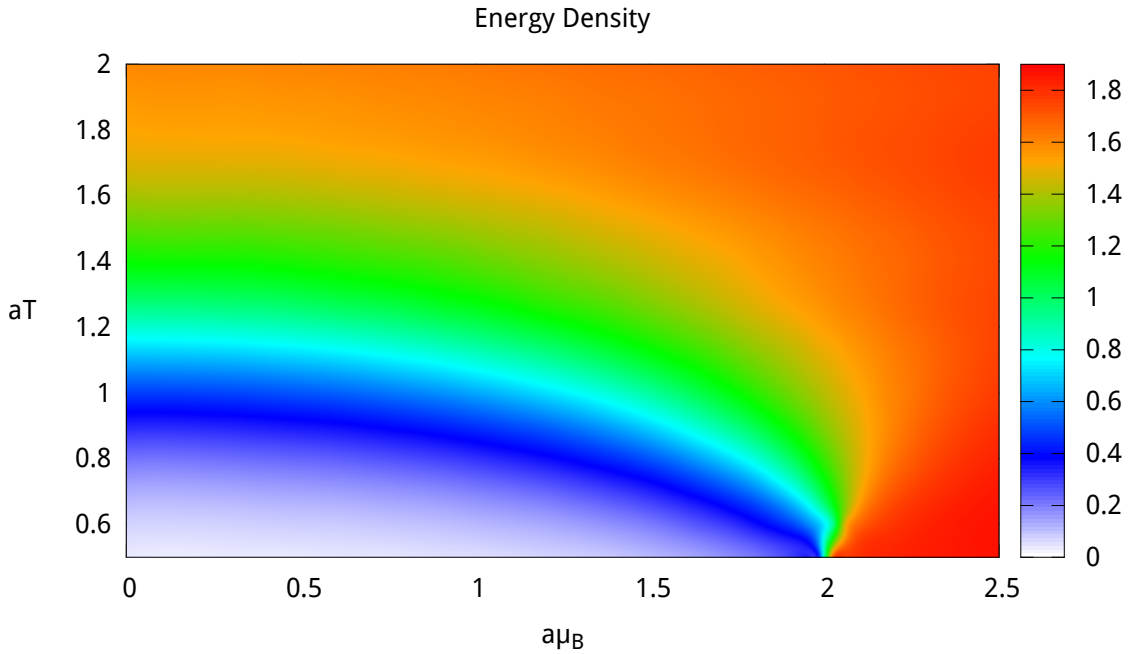

Figure 17: The energy density across the T, μ-plane for $am_q = 0.1$ as a heat map.

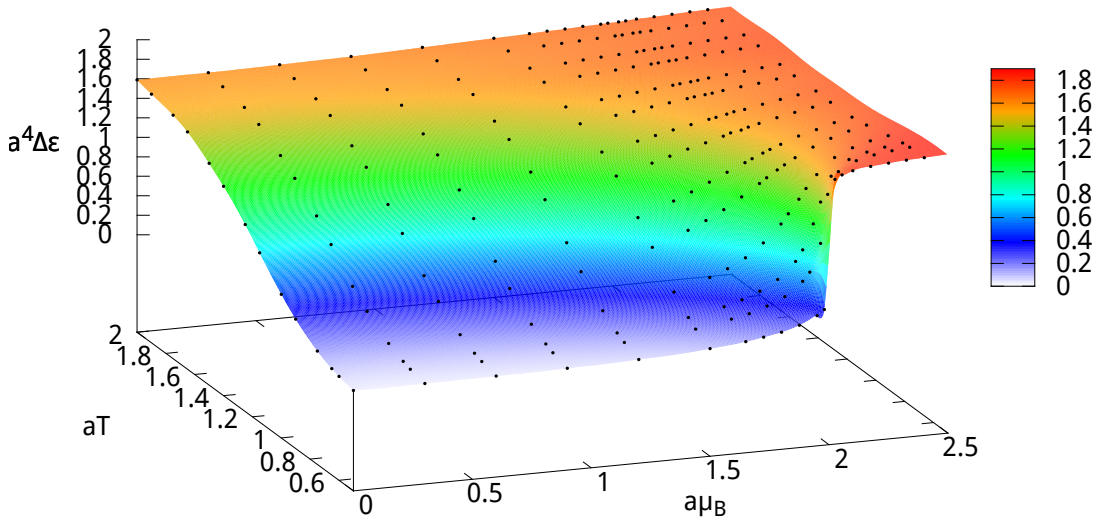

Figure 18: The energy density across the T, μ-plane for $am_q = 0.1$

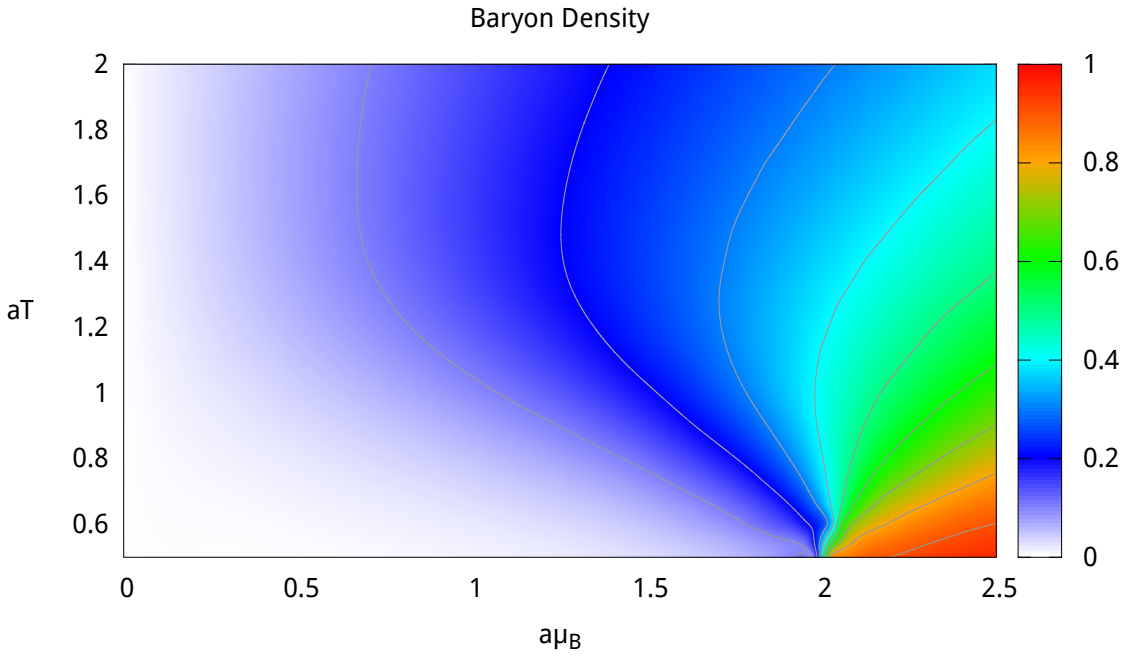

Figure 19: Baryon density $a^3 n_B$ across the T, μ-plane for $am_q = 0.1$ as a heat map.

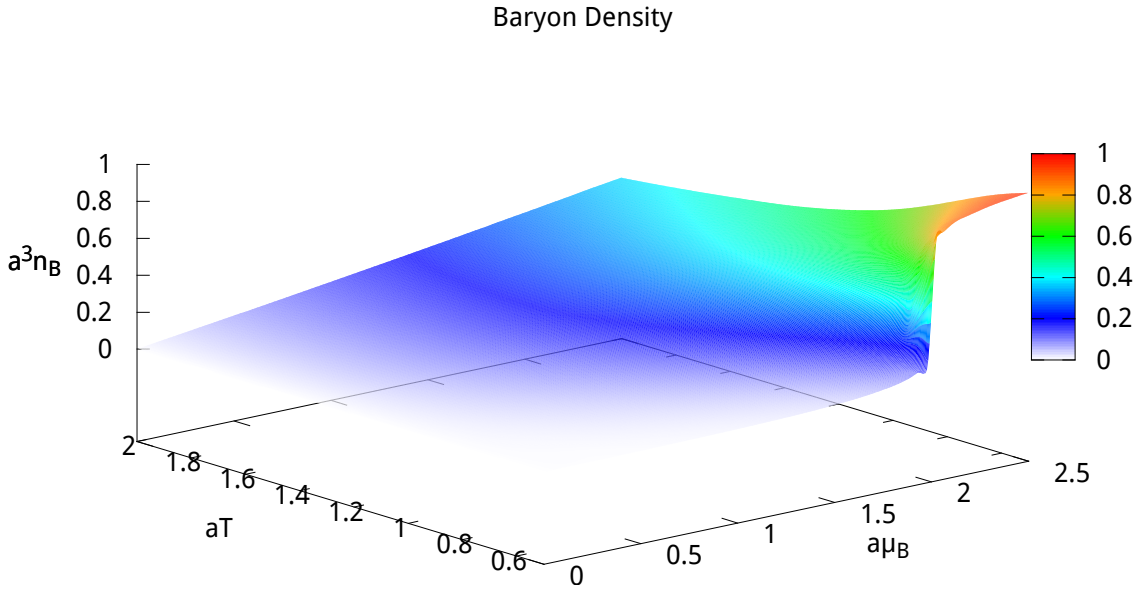

Figure 20: Baryon density $a^3 n_B$ across the T, μ-plane for $am_q = 0.1$.

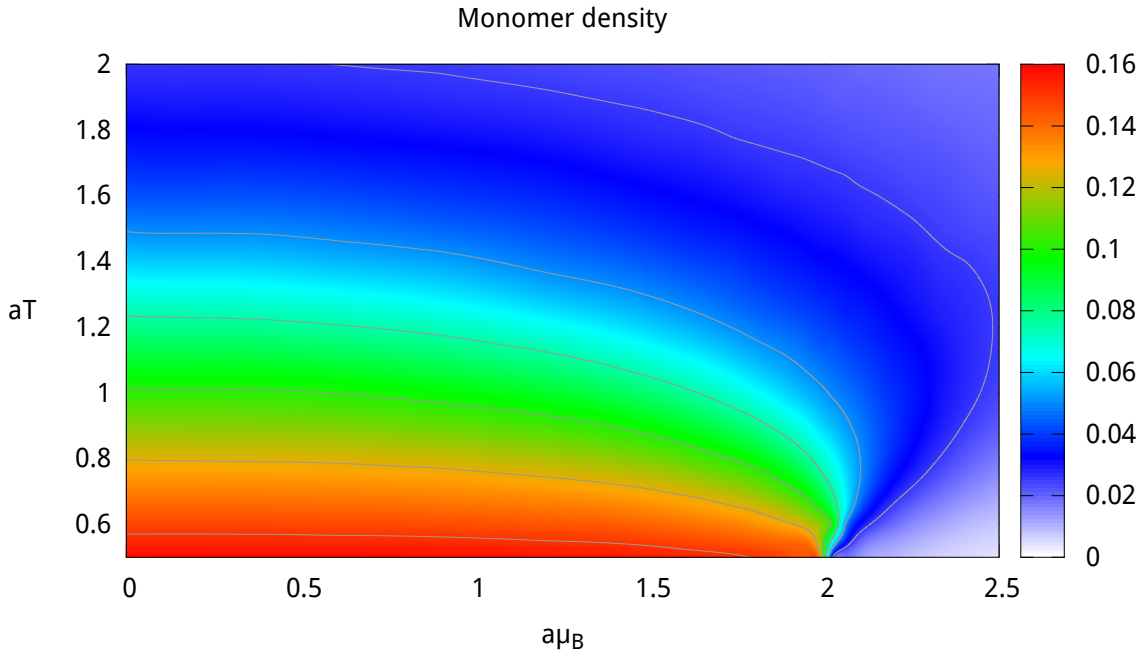

Figure 21: Monomer density $\langle n_M \rangle$ across the T, μ-plane for $am_q = 0.1$.

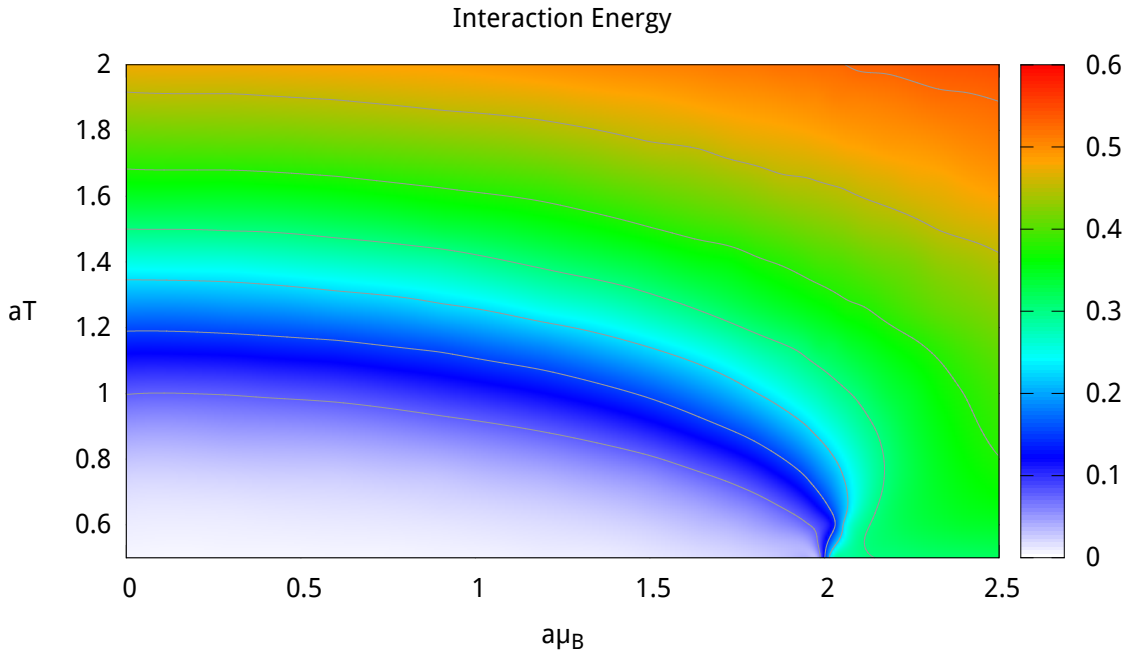

Figure 22: Interaction energy $a^4(\Delta\epsilon - 3\Delta p)$ across the T, μ-plane for $am_q = 0.1$.

The energy density, shown in Fig. 17 as a heat map, depicts interesting behaviour. At small chemical potentials up to $\mu = 1.0$, the energy density changes only mildly; the contour lines are almost parallel to the $a\mu$-axis and exhibit only a very small curvarture towards smaller temperatures. Above $\mu = 1.0$, the curvature slowly starts to increase up to the point $(aT, a\mu) \sim (0.6, 2)$. At this point, the different contour lines converge and are roughly parallel to the aT-axis. This line extends down to $aT = 0.5$ and across it, the energy density suddenly jumps from almost zero to its maximal value $a^4\Delta\epsilon_{\max} \sim 2$. Recalling the phase diagramm of strong coupling QCD, one sees that this is an imprint of the first order phase transition in the high density, low temperature region. The jump in the energy density across the phase boundary is exactly the latent heat needed to go from one phase to the other and $(aT, a\mu) \sim (0.6, 2)$, where the contour lines converge, corresponds to the second order end point seperating the crossover transition from the first order line. In the crossover region, the contour lines mimmic the crossover line. In Fig. 18, the same data is shown as a three dimensional plot where the thin plate spline interpolation is overlayed with the simulation results represented by black dots.

Fig. 19 shows the baryon density across the T, μ-plane. For small temperatures, the baryon density remains zero up to the critical chemical potential $a\mu_c \sim 2$ as expected from the silver blaze property. The baryon density then jumps across $a\mu_c$ to $a^3 n_B \sim 1$. Across this transition the system changes from a meson gas towards to a baryonic crystal, where the lattice is almost completely filled with baryon loops winding around temporal direction. In contrast to the energy density, there is no imprint of the chiral crossover line on the baryon density. The contour lines corresponding to densities $a^3 n_B < 0.5$ emerge from the small first order region and tend towards smaller chemical potentials up to temperatures around $aT = 1.3$ where they bend upwards and finally incline towards high chemical potentials. The detour into the left part of the T, μ-plane decreases with the baryon density and vanishes for contour lines with $a^3 n_B \geq 0.5$. For high temperatures the baryon density increases linearly with the chemical potential as seen in the three dimensional plot of the results in Fig. 20.

The monomer density is shown in Fig. 21. It has its maximum in the low temperature region with $\mu < \mu_c$ where the baryon density vanishes. Towards higher temperatures the density smoothly decreases but across the first order phase transition in μ direction it abruptly drops to zero - exactly where the baryon density is maximal.

Fig. 22 displays the interaction energy $\Delta\epsilon - 3\Delta p$ which is obtained from the vacuum subtracted monomer density and ξ. In contrast to the energy density, the interaction energy does not saturate in the high density - low temperature region. Apart from that, it resembles the behaviour of the energy density in the remaining part of the T, μ-plane.

The pressure is obtained by combining the results for the energy density and the interaction energy according to (6.4). A heat map of the results is given in Fig. 23. The behaviour is again very similar to the energy density. This is not surprising as the observables n_{D_t} and n_{B_t} are the main contributions to the pressure. This, however, has some serious consequences for the pressure. Just as the energy density, the pressure jumps rapidly across the first order phase transition as seen in Fig. 24. This is problematic as it is expected that the pressure is continuous across the transition. The problem of the discontinuous pressure will be discussed in more detail in the next section. For now, we want to conclude this section by discussing the quark mass dependence of the results. The energy density, baryon density and pressure for

the $am_q = 0.05$ case are shown in the figures Fig. 25, Fig. 26 and Fig. 27. The first order transition has shifted from $a\mu_c \sim 2$ to $a\mu_c \sim 1.8$. The observation at $\mu = 0$ that the energy density decreases with quark mass holds true apart from a small region in the T, μ-plane to the right of the transition where the energy density for the $am_q = 0.1$ case seems to be larger than the results for $am_q = 0.05$. The findings about the shift of $a\mu_c$ match [10], where the influence of a quark mass on the phase diagramm of strong coupling QCD was studied. There, it was found that with increasing quark mass the critical endpoint and the first order line move towards higher chemical potentials and lower temperatures.

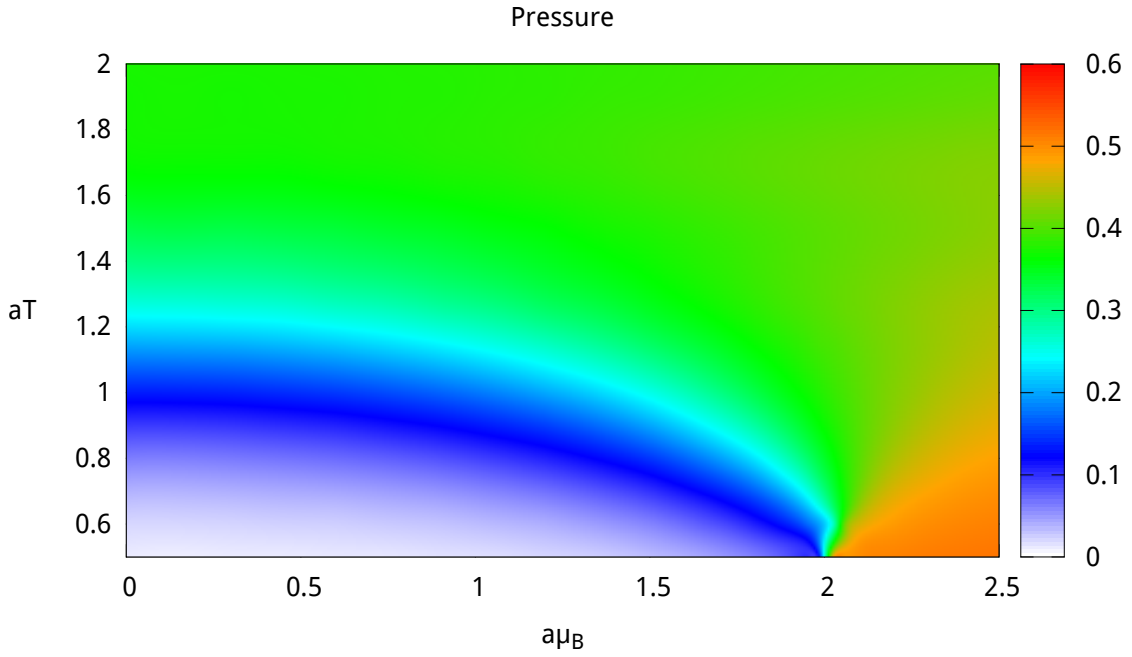

Figure 23: The pressure across the T, μ-plane for $am_q = 0.1$ as a heat map.

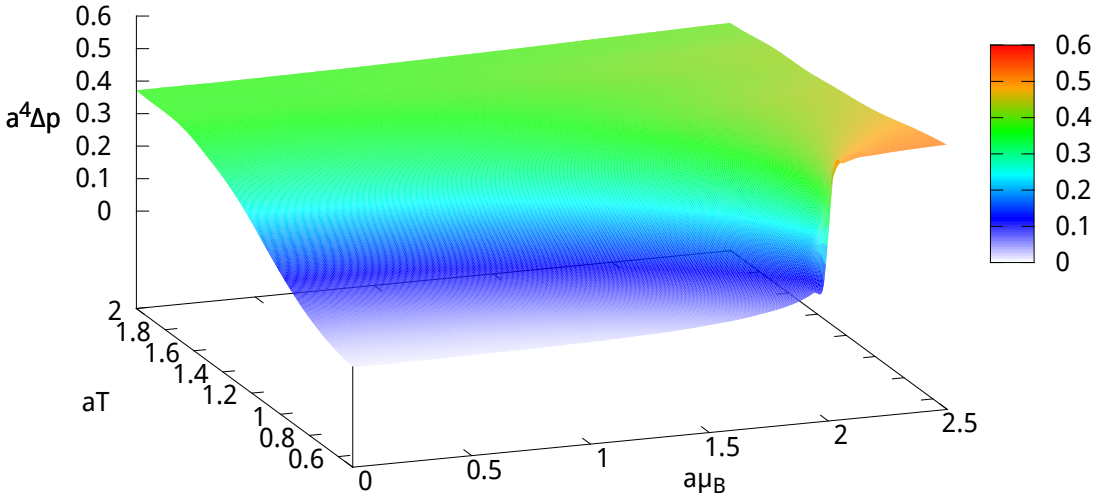

Figure 24: The pressure across the T, μ-plane for $am_q = 0.1$.

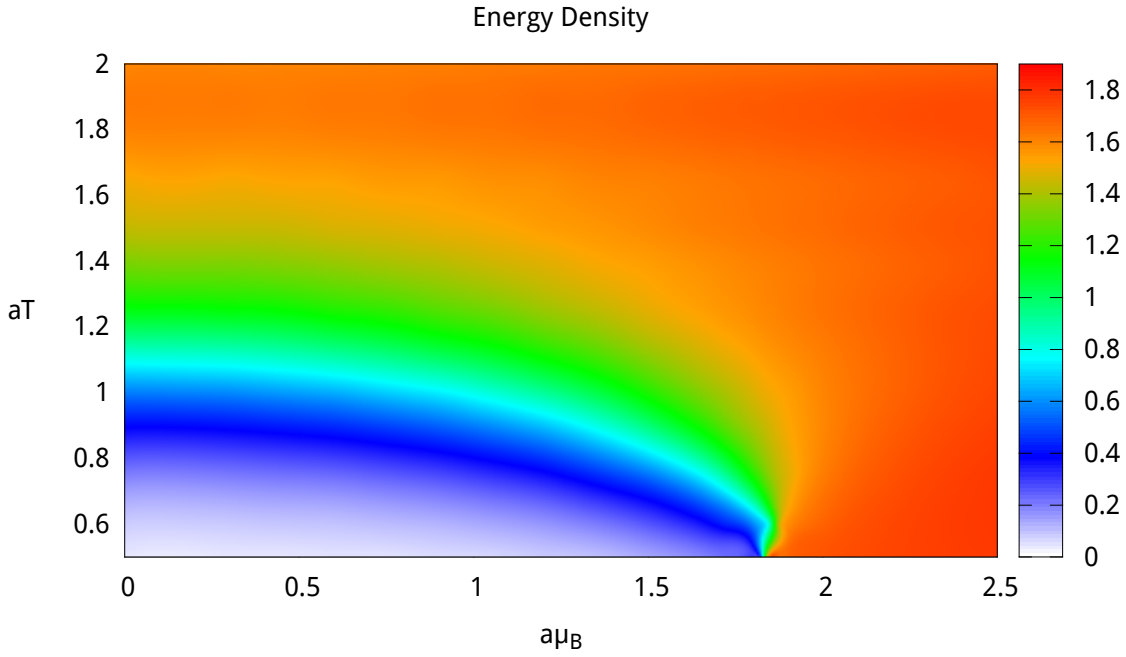

Figure 25: The energy density across the T, μ-plane for $am_q = 0.05$ as a heat map.

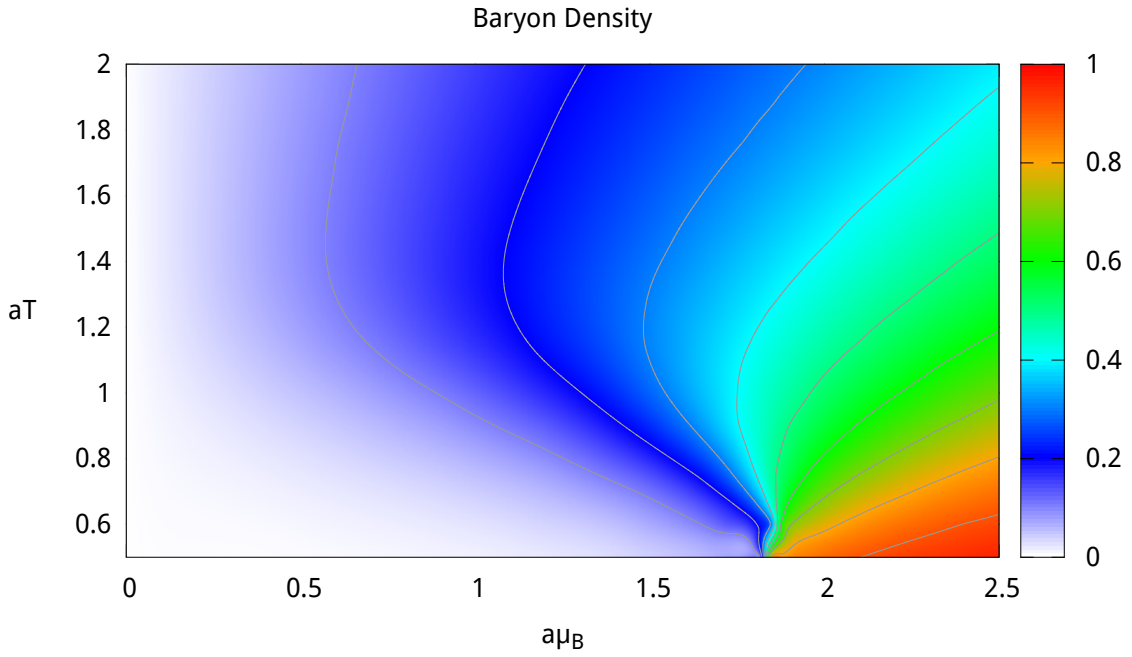

Figure 26: Baryon density $a^3 n_B$ across the T, μ-plane for $am_q = 0.05$.

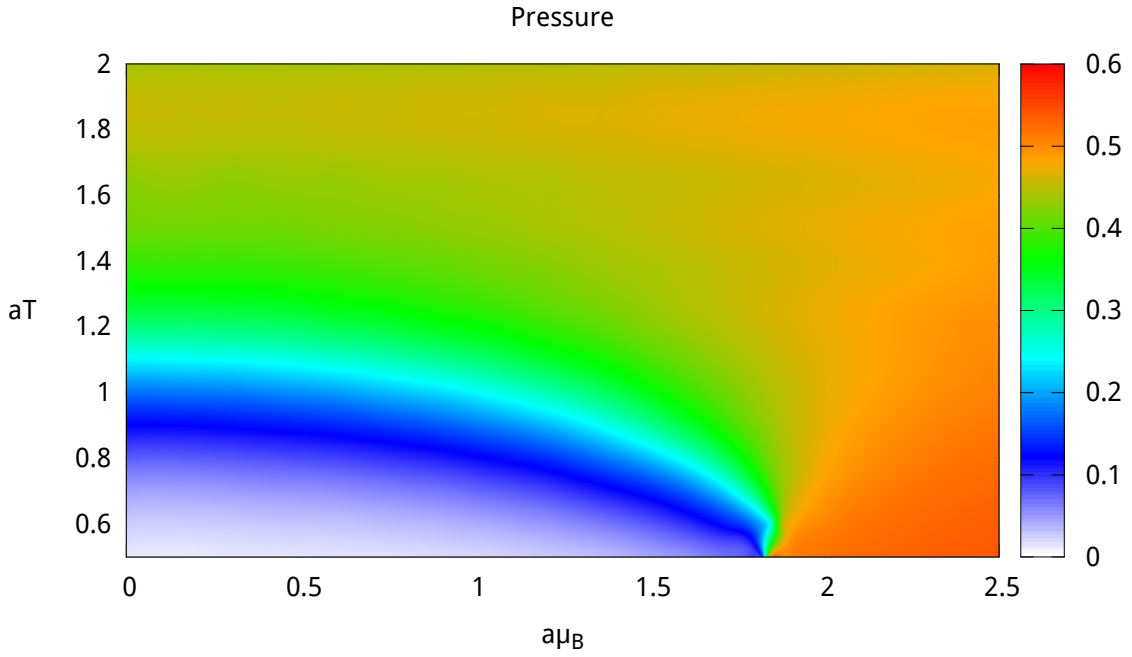

Figure 27: The pressure across the T, μ-plane for $am_q = 0.05$ as a heat map.

Discontinuous pressure

The pressure calculated according to (6.4) was found to be discontinuous across the first order phase transition. From (6.4), this is not surprising since the contributing observables $\langle 2n_{D_t} + 3n_{B_t}\rangle$ and $\langle n_M\rangle$ are related to first derivatives of the grand canonical potential Φ which can be singular[9] at a first order phase transition. The thermodynamic potential itself, however, has to be continuous across the phase transition. Under the assumption that Φ is homogeneous in the volume, that is

$$\Phi(T, \alpha V, \mu) = \alpha\Phi(T, V, \mu) \tag{6.16}$$

the pressure is a thermodynamic potential

$$p = \frac{T}{V}\log Z, \tag{6.17}$$

which is readily seen by differentiating (6.16) with respect to α:

$$\begin{aligned}
\frac{\partial}{\partial\alpha}\Phi(T, \alpha V, \mu) &= \frac{\partial}{\partial\alpha}\alpha\Phi(T, V, \mu)\\
\frac{\partial\alpha V}{\partial\alpha}\frac{\partial\Phi(T, \alpha V, \mu)}{\partial\alpha V} &= \Phi(T, V, \mu)\\
V\frac{\partial\alpha\Phi(T, V, \mu)}{\partial\alpha V} &= V\frac{\partial\Phi(T, V, \mu)}{\partial V} = -Vp = \Phi(T, V, \mu).
\end{aligned}$$

Therefore, the pressure has to be continuous across the first order phase transition. The homogeneity condition (6.16) is usually assumed to hold in the case of QCD. This problem with the determination of the pressure is not new. In early works on finite temperature lattice QCD, the calculation of the pressure on anisotropic lattices resulted in negative pressure or pressure gaps across first order transitions, which were attributed to the use of perturbatively determined anisotropy coefficients. The usage of non-perturbatively renormalized coefficients resolves this problem [15]. In our case, we used a non-perturbative renormalization prescription to calculate $\xi(\gamma)$ but neglected the effects of baryons because of the large computational effort. One might argue that the determination of $\xi(\gamma, \mu \neq 0)$ is necessary around the first order transition since the sudden jump in baryon density might have a strong effect on the fluctuations of the conserved charges.

6.4. Going beyond $\beta_G = 0$

A long term goal of the dual variable approach is to move away from the strong coupling limit and include the effect of gluons correctly. The current pursued strategy is to expand the gauge action in terms of the inverse gauge coupling β_G around $\beta_G = 0$. The 0^{th}-order corresponds to the strong coupling limit discussed in this thesis. For higher order corrections, the link integral discussed before obtains new contributions from powers of $\mathrm{Tr}\left[U_P + U_P^\dagger\right]$. These

[9] i.e. discontinuous or divergent.

integrals can be computed in closed form but the subsequent contraction of the free indices and the grassmann integration remains challenging. A dual formulation including next-to-leading order gauge corrections was constructed in [6]. In addition to the monomer, dimer and baryon loop degrees of freedom in the strong coupling case, further integer variables are introduced: the plaquette and anti-plaquette occupation numbers n_P and $\bar{n}_P$, which arise from powers of $\mathrm{Tr}[U_P]^{n_P}$ and $\mathrm{Tr}[U_P]^\dagger$. The partition function in this new dual variables reads

$$Z = \sum_{\{n_x,k_b,l_{N_c},n_P,\bar{n}_P\}} \prod_{b=(x,\mu)} \frac{(N_c-k_b)!}{N_c!\,(k_b-|f_b|)!}\gamma^{(2k_b-f_b)\delta_{0\mu}} \prod_x \frac{N_c!}{n_x!}\left(2am_q\right)^{n_x} \tag{6.18}$$
$$\times \prod_{l_{N_c},l_f} w(l_{N_c},l_f,\mu) \prod_P \frac{\left(\frac{\beta_G}{2N_c}\right)^{n_P+\bar{n}_P}}{n_P!\bar{n}_P!},$$

where the auxiliary variables f_b, f_x and l_f are

$$f_b = \sum_{P\in P_b^+}(n_P-\bar{n}_P) + \sum_{P\in P_b^-}(\bar{n}_P-n_P) \in \{0,\pm 1\},$$
$$f_x = \frac{1}{2}\sum_b |f_b| \in \{0,1\} \quad \text{and}$$
$$l_f = \{b=(x,\mu)|f_b = \pm 1 \text{ are connected}\}.$$

In the presence of gauge corrections, the Grassmann constraint is modified[10] to the so-called color constraint

$$n_x + \sum_{\hat{\mu}=\pm 0,\ldots,\pm\hat{d}} \left(k_{\hat{\mu}}(x) + \frac{N_c}{2}|l_{N_c,\hat{\mu}}(x)|\right) = N_c + f_x.$$

The inclusion of gauge corrections also impacts the determination of thermodynamic observables like energy density and pressure and their calculation becomes highly non-trivial. One of the tricks used to calculate derivatives with respect to temperature or volume was to recast them in terms of derivatives of the anisotropy coupling. This necessitated the determination of the running of the anisotropy coupling. With the introduction of another bare parameter, the inverse gauge coupling β, the effect of this coupling onto the anisotropy has to be taken into account as well. The energy density in the presence of next-to-leading order gauge corrections reads

$$a^4\epsilon = \frac{\xi^2}{\gamma}\frac{\partial\gamma}{\partial\xi}\left(\langle 2n_{k_t} - n_{f_t}\rangle + 3\langle n_{B_t}\rangle\right) - \xi^2\frac{2N_c}{\beta_G}\frac{\partial\beta_G}{\partial\xi}\langle n_P+\bar{n}_P\rangle. \tag{6.19}$$

Here, n_{f_t} is the density of the auxiliary variable f_b which is determined by the plaquette occupation numbers. The pressure receives a similar contribution from the plaquette occupation numbers. This new contribution gives us an interesting prospect even for the strong coupling

[10]There are also modifications to the baryonic weights, but they are of no concern for the following discussion.

limit. If the strong coupling limit is approached from $\beta_G > 0$, thereby taking the plaquette occupation numbers into account, the result might be significantly different compared to starting directly at $\beta_G = 0$. The average plaquette $\left\langle \mathrm{Tr}\left(U_P + U_P^\dagger\right)\right\rangle$ is equivalent to $\langle n_P + \bar{n}_P\rangle$ in the strong coupling limit and is, in fact, non-zero as seen in 28. Depending on the behavior of $\frac{1}{\beta_G}\frac{\partial\beta}{\partial\xi}$ in the limit $\beta_G \to 0$[11], one might obtain important contributions from the gauge sector even in the strong coupling limit.

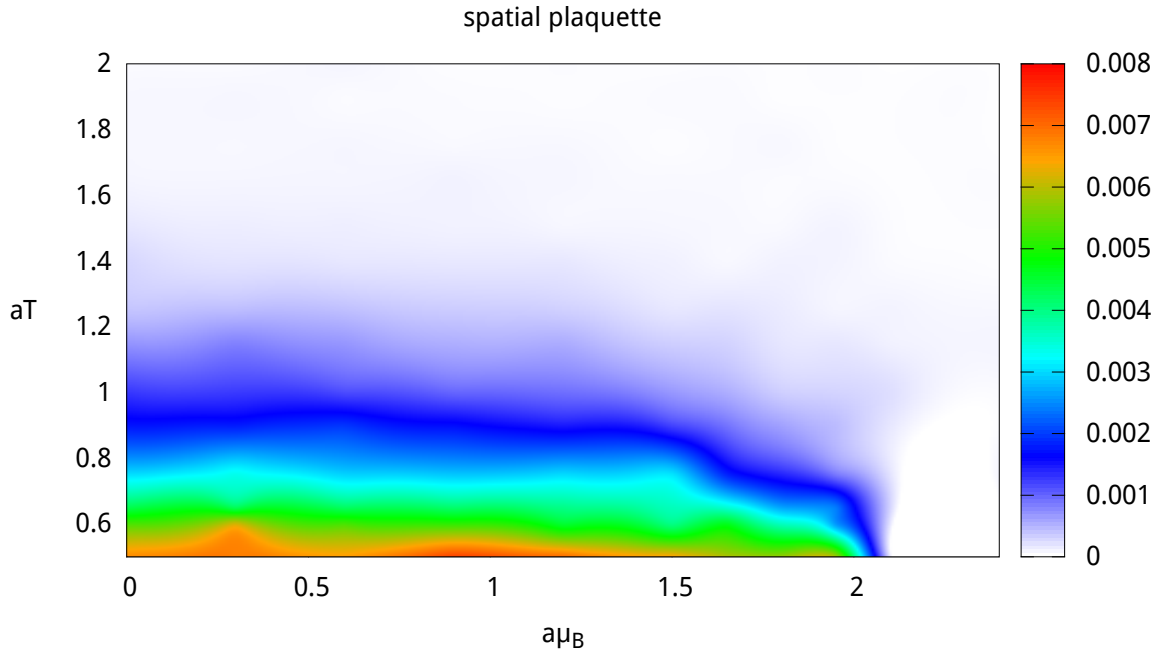

Figure 28: Average spatial plaquette on $10^3 \times 4$ lattices across the T, μ-plane.

[11] That hopefully exists!

7. Baryon density fluctuations

As we have seen in the various results of the previous section, the dual formulation of strong coupling QCD allows us to soften the sign problem enough to perform simulations across the full T, μ-plane. Furthermore, the complete phase diagram of strong coupling QCD can be calculated in the dual formulation [16],[17]. In conventional QCD simulations, the finite density region can only be accessed by extrapolation-based methods from the $\mu = 0$ region. It is therefore interesting to use strong coupling QCD as a toy-model to test commonly used methods of full QCD at finite density. The most prominent method of these is the Taylor expansion of the pressure in $\frac{\mu_B}{T}$[12], which leads to a series in higher order cumulants of the baryon density distribution. Besides access to finite density physics, this method is also used in the search for the critical endpoint of QCD. The radius of convergence of the Taylor series is limited by the pole of $\log Z$ closest to the origin which might be used to constrain the location of the critical endpoint. For strong coupling QCD, the location of the critical endpoint is known [10] so that one could validate the bounds on its location obtained from the radius of convergence. Motivated by the precision of the previous results, we want to explore how far the Taylor expansion can reach with our methods for strong coupling QCD.

7.1. Setup

Assuming the homogeneity condition (6.16) holds, we expand the pressure p in $\frac{\mu_B}{T}$ around $\mu = 0$

$$p = \frac{T}{V} \log Z = p(T,0) + \frac{T}{V} \sum_{n=1}^{\infty} \frac{1}{(2n)!} \left(\frac{\mu_B}{T}\right)^{2n} \left. \frac{\partial^{2n} \log Z}{\partial(\mu_B/T)^{2n}} \right|_{\mu_B=0}.$$

The $U(1)$ symmetry related to baryon number conservation implies that the thermodynamic potential has to be an even function of μ_B such that all odd derivatives with respect to μ_B vanish at $\mu_B = 0$. The n-th derivative with respect to the chemical potential will yield the n-th cumulant of the winding number $\kappa_n(r_l)$ so that we obtain

$$\begin{aligned} \Delta p = p(T,\mu_B) - p(T,0) &= \frac{T}{V} \sum_{n=1}^{\infty} \frac{1}{(2n)!} \left(a_\tau N_\tau \mu_B\right)^{2n} \left. \frac{\partial^{2n} \log Z}{\partial(a_\tau N_\tau \mu_B)^{2n}} \right|_{\mu_B=0} \\ &= \frac{1}{a^3 a_\tau N_\tau N_\sigma^3} \sum_{n=1}^{\infty} \frac{1}{(2n)!} \left(a_\tau N_\tau \mu_B\right)^{2n} \kappa_{2n}(r_l). \end{aligned}$$

We multiply with $a^3 a_\tau$ and $\xi(\gamma) = \frac{a}{a_\tau}$ and use $\kappa_n(r_l) = (N_\sigma^3)^n \kappa_n(\omega_l)$ to obtain

$$a^4 \Delta p = \sum_{n=1}^{\infty} \frac{\left(a_\tau \mu_B\right)^{2n}}{(2n)!} \xi \left(N_\tau N_\sigma^3\right)^{2n-1} \kappa_{2n}(\omega_l). \tag{7.1}$$

[12] In modern approaches, a simultaneous expansion in the three chemical potentials μ_B (baryon), μ_S (strangeness) and μ_Q (charge) is performed, see [18]

The cumulants $\kappa_n(\omega_l)$ cannot be measured directly, but one may use their relation to the moments $\mu_n(\omega_l) = \langle \omega_l^n \rangle$. The first four even cumulants expressed in terms of the moments read:

$$\begin{aligned}
\kappa_2 &= \mu_2 - \mu_1^2 \qquad (7.2)\\
\kappa_4 &= -6\mu_1^4 + 12\mu_1^2\mu_2 - 3\mu_2^2 - 4\mu_1\mu_3 + \mu_4\\
\kappa_6 &= -120\mu_1^6 + 360\mu_2\mu_1^4 - 120\mu_3\mu_1^3 - 270\mu_2^2\mu_1^2 + 30\mu_4\mu_1^2 + 120\mu_2\mu_3\mu_1 - 6\mu_5\mu_1\\
&\quad + 30\mu_2^3 - 10\mu_3^2 - 15\mu_2\mu_4 + \mu_6\\
\kappa_8 &= -5040\mu_1^8 + 20160\mu_2\mu_1^6 - 6720\mu_3\mu_1^5 - 25200\mu_2^2\mu_1^4 + 1680\mu_4\mu_1^4 + 13440\mu_2\mu_3\mu_1^3\\
&\quad - 336\mu_5\mu_1^3 + 10080\mu_2^3\mu_1^2 + 1680\mu_3^2\mu_1^2 - 2520\mu_2\mu_4\mu_1^2 + 56\mu_6\mu_1^2 - 5040\mu_2^2\mu_3\mu_1 + 560\mu_3\mu_4\mu_1\\
&\quad + 336\mu_2\mu_5\mu_1 - 8\mu_7\mu_1 - 630\mu_2^4 + 560\mu_2\mu_3^2 - 35\mu_4^2 + 420\mu_2^2\mu_4 - 56\mu_3\mu_5 - 28\mu_2\mu_6 + \mu_8.
\end{aligned}$$

7.2. Analytical crosschecks

The numerical evaluation of the cumulants becomes increasingly difficult with higher orders since there are a lot of cancellations present in the above formulae. To check whether our numerical methods work correctly and to develop an expectation for the results on larger lattices, we first perform analytical crosschecks on small lattices where the partition function can be calculated by hand. To keep the number of configurations manageable, we calculate Z on a 2^2 lattice in the chiral limit $am_q = 0$ so that only dimers and baryons are present.
The configurations can be classified by the winding number $r_l = -2, -1, 0, 1, 2$ and we split the partition function into

$$Z_{2\times 2} = Z_{r_l=2} + Z_{r_l=1} + Z_{r_l=0} + Z_{r_l=-1} + Z_{r_l=-2}.$$

The contributions $Z_{r_l=2}$ and $Z_{r_l=-2}$ are given by the two purely baryonic configurations shown in Fig. 29.

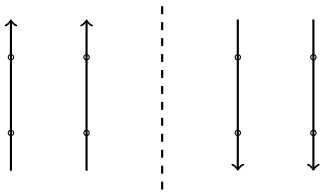

Figure 29: Configurations contributing to $Z_{r_l=2}$ (left) and $Z_{r_l=-2}$ (right).

The $r_l = \pm 1$ sector is already significantly larger and consists of eight pure baryonic loops and eight mixed contributions. They are shown in Fig. 30.

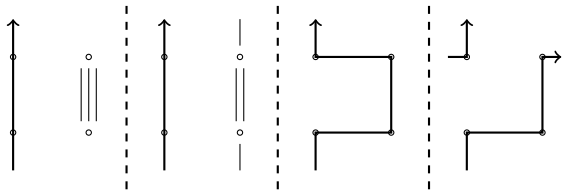

Figure 30: Configurations contributing to $Z_{r_1=1}$ up to shifts and reflections. The $r_l = -1$ sector is obtained by reversing the baryon flux.

The largest number of configurations is found in the $r_l = 0$ sector. It can be separated further into a purely baryonic sector, a mixed sector and a purely mesonic sector. The mixed sector contains the same mixed configurations as $Z_{r_l=1}$ and $Z_{r_l=-1}$ but rotated into the spatial direction. Similarly, the baryonic sector consists of rotations of the baryonic loops found in $Z_{r_l=\pm 2}$ and $Z_{r_l=\pm 1}$ and twelve new configurations. Four of which consist of two straight baryon loops facing in opposing directions and the remaining eight consist of a baryon loop wrapping around an elementary cell. The purely mesonic sector is the largest and contains more than 100 dimer configurations. In Fig. 31, examples of configurations contributing to $Z_{r_l=0}$ are shown.

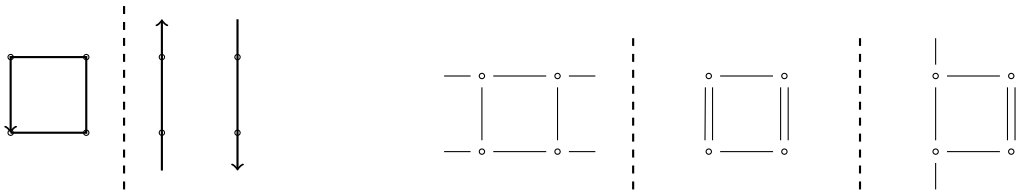

(a) New, purely baryonic configurations that are not rotations of $r_l = \pm 2$ or $r_l = \pm 1$.

(b) Exemplary mesonic configurations.

Figure 31: Exemplary configurations contributing to $Z_{r_l} = 0$.

After weighting all configurations according to (4.10), the partition function reads

$$Z_{2\times 2} = \gamma^{12}\left(4\cosh(\mathrm{e}^{2\mu_B/T}) + 16\cosh(\mathrm{e}^{\mu_B/T}) + 16\right) + \frac{400}{9}\left(\gamma^8 + \gamma^4\right) + 4. \tag{7.3}$$

From here, we calculate the moments of n_B by taking derivatives with respect to the baryon chemical potential μ_B and combine them via (7.2) into cumulants of up to order eight. Additionally, we perform quick simulations on 2×2 lattices to check that our data analysis works properly. The results are shown in Fig. 32 and Fig. 33.

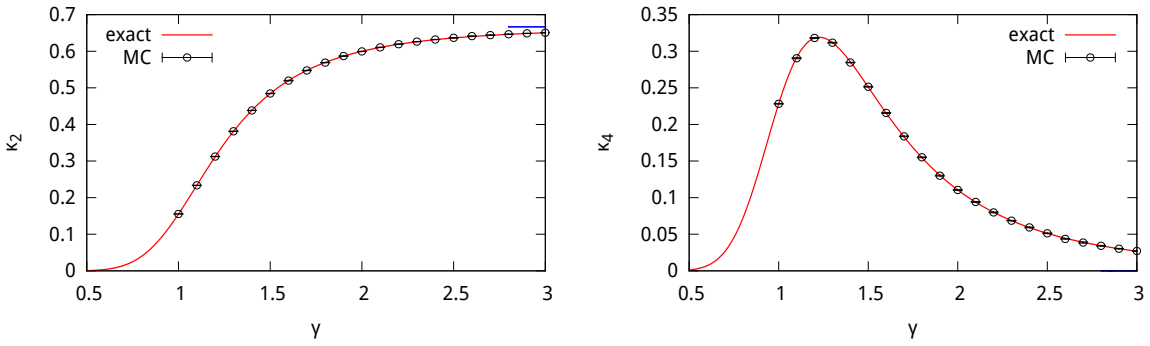

Figure 32: Left: κ_2 as a function of γ as obtained from $Z_{2\times 2}$ (red) and from Monte Carlo simulations (black). Right: κ_4 as a function of γ. The blue line corresponds to the $\gamma \to \infty$ limit.

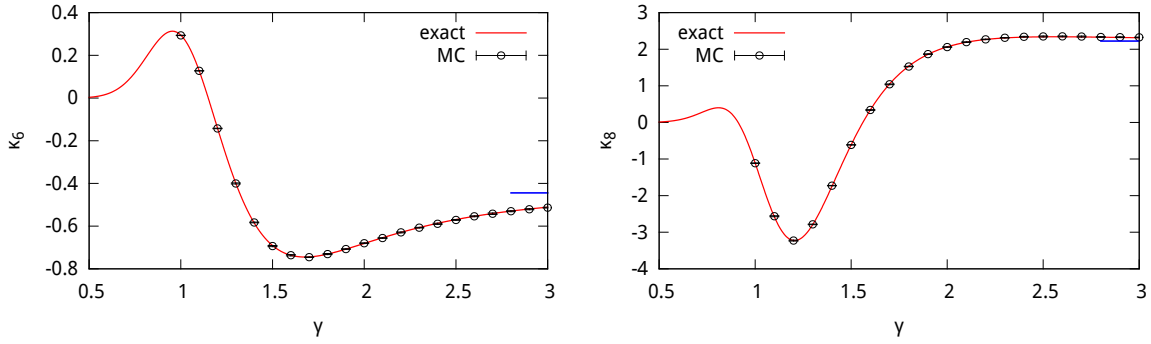

Figure 33: κ_6 and κ_8 versus γ.

In all four cases, the Monte Carlo result matches the exact result perfectly. Interestingly, we find that the cumulants roughly fulfill

$$\frac{\partial^2}{\partial \mu_B^2} \sim \frac{\partial}{\partial \gamma},$$

i.e. the fourth order cumulant behaves like the derivative of the second order cumulant. The peak of κ_4 roughly coincides with the inflection point of κ_2. Similarly, κ_2 possesses no local extremum whereas κ_4 possesses one, κ_6 possesses two and κ_8 possesses three. For $\gamma \to \infty$, all four cumulants approach a limiting value that can be calculated from the one-dimensional partition sum[13]

$$Z_2 = \gamma^6 \left(2\cosh(\mathrm{e}^{\mu_B/T}) + 4\right)$$

raised to the power $V_s = 2$. This is due to the fact that the partition function is dominated by configurations where dimers and baryons are oriented in temporal direction at high γ. The argument holds independent of the dimension of the original lattice. To predict the high temperature behavior of our $10^3 \times 4$ simulations, it suffices to calculate the partition function of a one dimensional lattice with $N_\tau = 4$. There are again only six configurations in this case: two baryon loops, two triple dimer chains and two 2-1 dimer chains. They are sketched below.

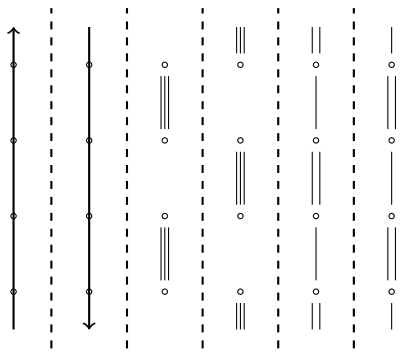

Figure 34: Configurations contributing to Z_4.

[13]There are only 6 configurations on a one dimensional lattice with $N_\tau = 2$. Two baryon loops, two triple dimer configurations and two 2-1 dimer chains.

The resulting partition function for these configurations is

$$Z_4 = \gamma^{12} \left(2\cosh(\mathrm{e}^{\mu_B/T}) + 4\right), \tag{7.4}$$

which we will compare to simulations in the next section.

7.3. Results

With all the preliminary work done, we want to turn to the actual simulations in $3+1$ dimensions. Again, we choose $10^3 \times 4$ lattices with $am_q = 0.1$. Since there are no zero temperature subtractions to perform here, the restriction $\xi \cdot 10 \in \mathbb{N}$ no longer applies and we choose $\xi \in \{1.0, 1.25, \ldots, 12\}$. Compared to the previous simulations, were a number of configurations between $8 \cdot 10^4$ and $1.6 \cdot 10^5$ sufficed to obtain very accurate results, the cumulants are significantly harder to measure and we used up to $1.2 \cdot 10^6$ configurations. The results for the second and fourth order cumulants are shown in Fig. 35 and 36. As before, the blue line indicates the $T \to \infty$ value obtained from (7.4).

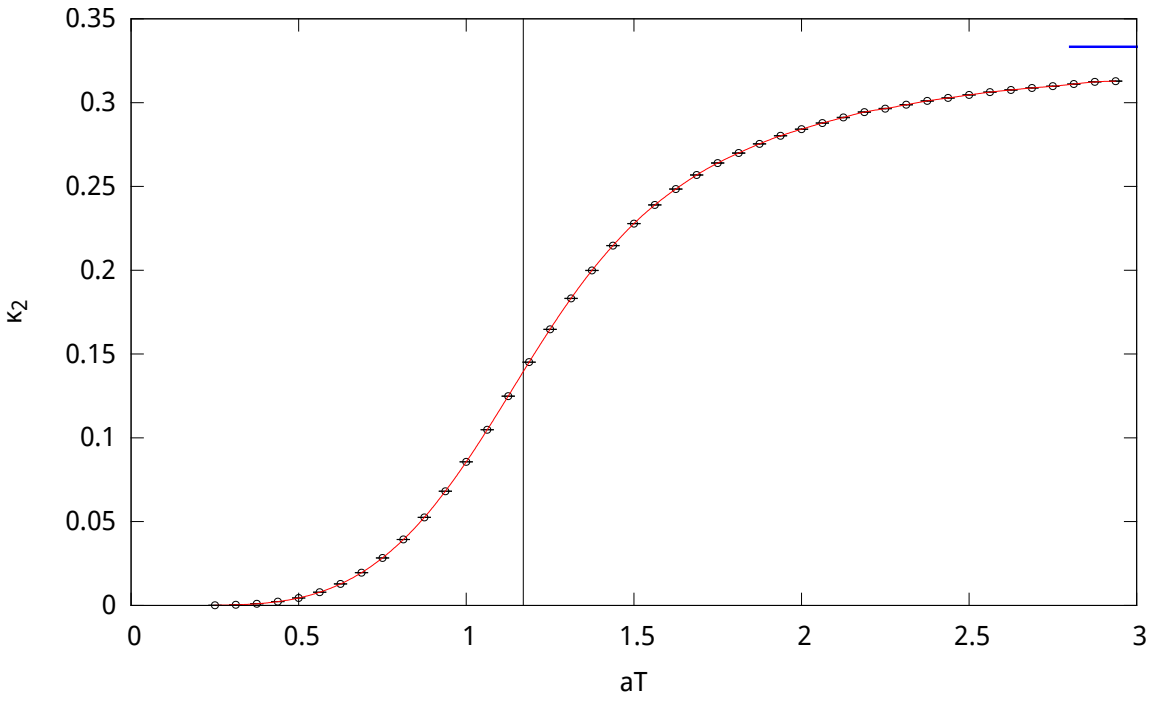

Figure 35: Second order cumulant κ_2 on a $10^3 \times 4$ lattice with $am_q = 0.1$. The black line corresponds to the crossover temperature estimated from the inflection point of the energy density, see Fig. 41 in the appendix.

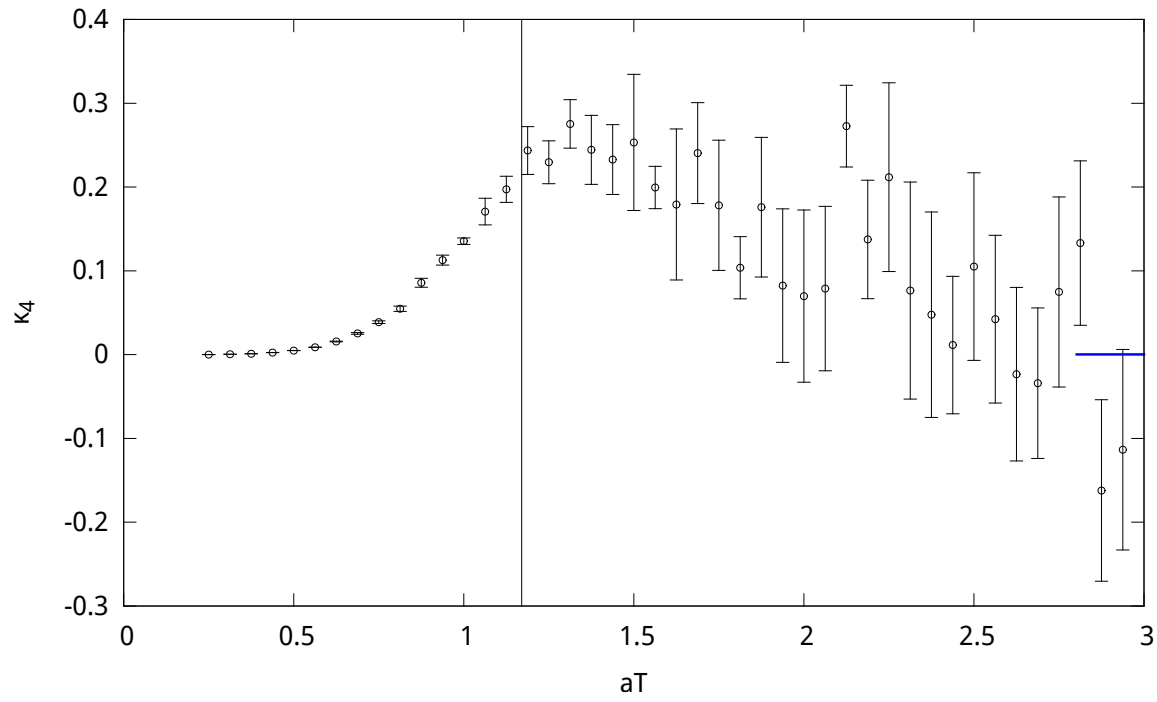

Figure 36: Second order cumulant κ_4 on a $10^3 \times 4$ lattice with $am_q = 0.1$.

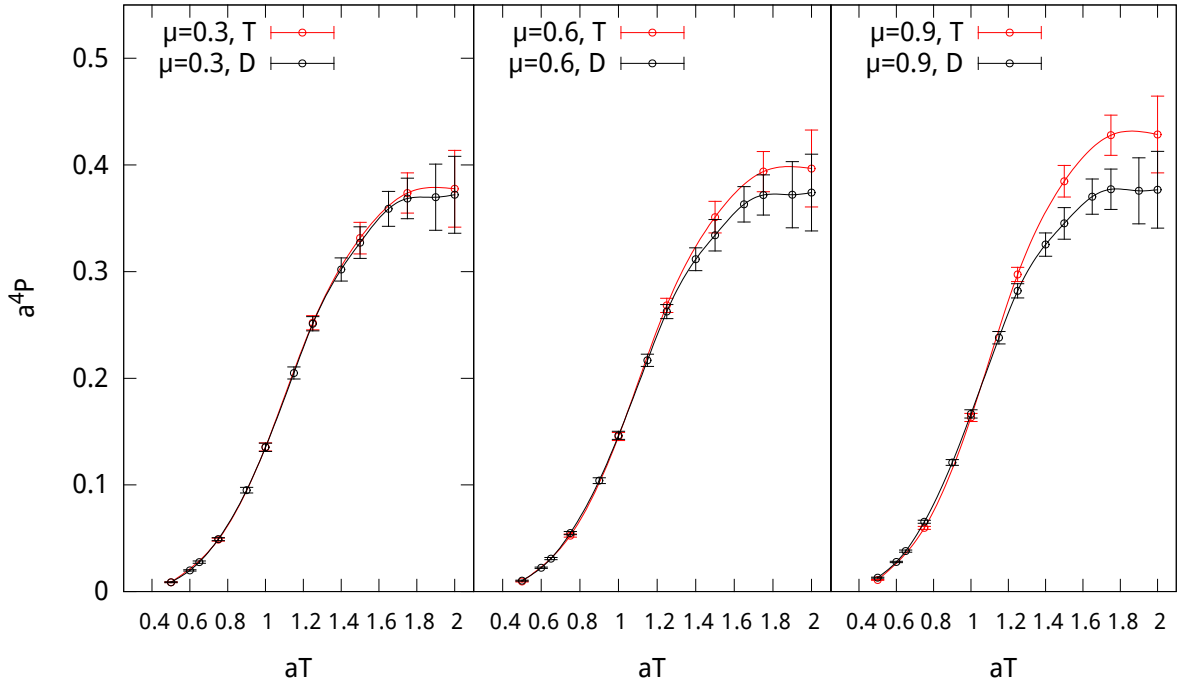

Figure 37: Red: Reconstruction of the pressure using the baryon density cumulants. Black: Results for the pressure from direct simulations at $\mu_B \neq 0$.

The second order cumulant shows exactly the behavior expected from the previous section. Its inflection point is roughly around the crossover temperature and for large temperatures, the $T \to \infty$ value predicted from (7.4) is approached. The fourth order cumulant, however, turns out to be very noisy. The statistical uncertainties grow drastically with temperature and the peak structure expected from the previous section is only vaguely recognizable. This uncertainty is partly due to the fact that larger temperatures cause longer run-times of the updating algorithm because large baryon loops are more frequent.
To reconstruct the pressure from these results, we combine (7.1) with the $p(T, \mu_B = 0)$ data. The reconstructed pressure for fixed chemical potentials is shown in Fig. 37. In Fig. 38, the same results are shown for fixed temperature instead.

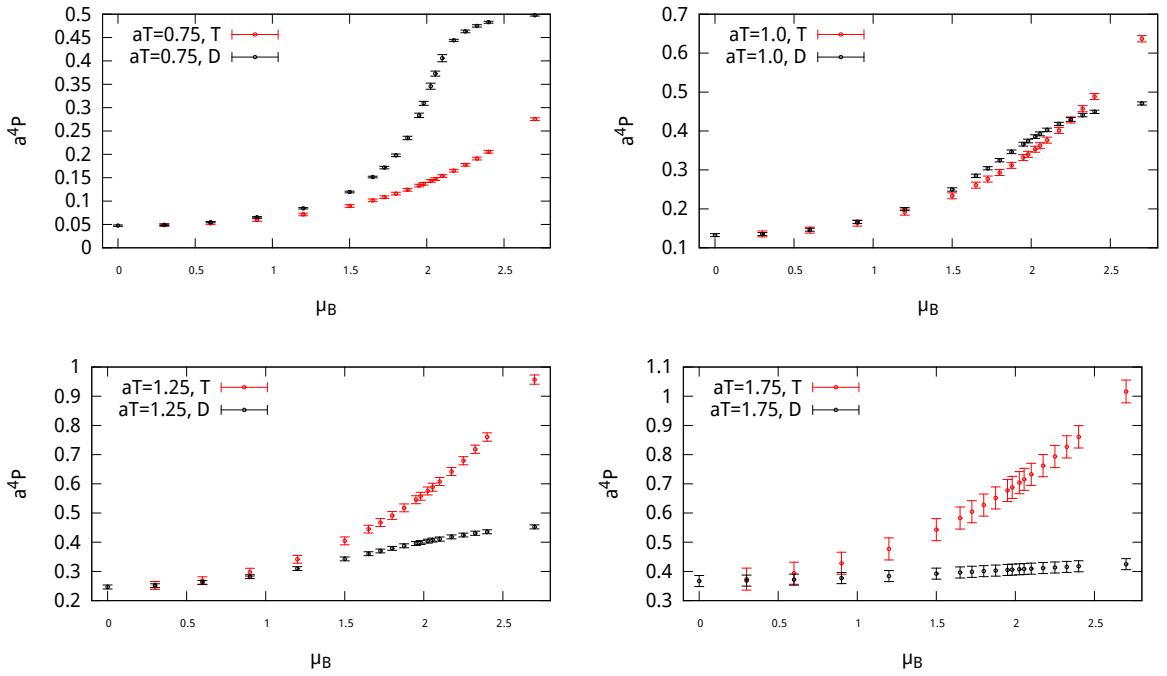

Figure 38: Red: Reconstructed pressure versus chemical potential for fixed aT. Black: Results from direct simulations.

Up to chemical potentials of around $a\mu_B = 0.9$, the reconstruction from the taylor expansion matches the direct simulations well. Beyond $a\mu_B = 0.9$, the taylor expansion starts to deviate notably from the direct simulations. For low temperatures, the reconstruction generally underestimates the pressure as seen in the top two panels of Fig. 38. At temperatures above $aT = 1.0$, the reconstruction overshoots the results from direct simulations.
For completeness, we also present the ratio of the two cumulants in Fig. 39. Together with a few more cumulants, one might use the ratios of subsequent Taylor coefficients c_n to estimate the radius of convergence via

$$\rho = \lim_{n\to\infty} \sqrt{\left|\frac{c_n}{c_{n+2}}\right|}.$$

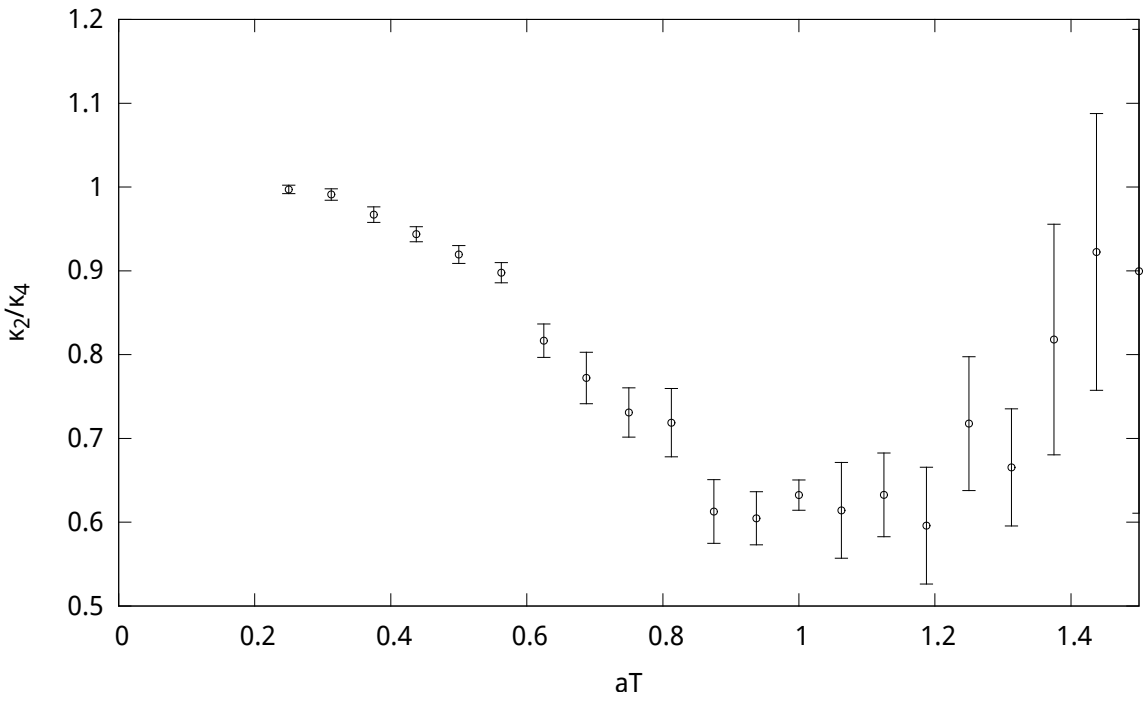

Figure 39: The ratio $\frac{\kappa_2}{\kappa_4}$ as a function of the temperature.

8. Summary

In this thesis, we used the dual representation of strong coupling lattice QCD with $N_f = 1$ to obtain insights on the bulk thermodynamic properties at finite density. Starting with the massless $U(3)$ case, we calculated the energy density of this purely mesonic system. We found that the energy density is very well described by the Stefan-Boltzmann law indicating that the system behaves like a non-interacting gas of massless mesons. Adding baryons to the system by switching the gauge group to $SU(3)$ changed this behaviour only slightly for higher temperatures and indicated that baryons are largely surpressed at $a\mu_B = 0$. By including a finite quark mass, we were able to observe a roughly exponential supression of the energy density with am_q for small to intermediate temperatures. Especially for high temperatures $aT > 1.4$, this gradually changed to a linear supression. With the introduction of the baryon chemical potential $a\mu_B$, we calculated the energy-, baryon- and monomer density across the full T, μ-plane and found that the strong coupling QCD phase diagramm left an imprint on all these quantities. While the energy density and monomer density contain imprints of both the crossover and the first order transition, only the latter is visible in the baryon density since the nuclear and chiral first order transitions coincide in strong coupling QCD. The gap in the energy density that we identified with the latent heat across the first order transition turned out to be problematic for the determination of the pressure. As both observables are made up of very similar operators, the pressure exhibits a similar gap across the first order transition. We speculated that this unphysical behaviour might be due to the approximations that were made for the calibration of the anisotropy $\xi(\gamma)$. Beyond μ_c, the influence of baryons on ξ should not be neglected. We also repeated the calculations for a slightly smaller quark mass of $am_q = 0.05$ and found qualitative agreement with the result from [10] that the critical endpoint wanders to higher μ and smaller T for increasing quark mass. Lastly, we discussed how gauge corrections would influence the calculation of ϵ and related quantities. Most notably, the anisotropy calibration becomes much more challenging and new observables contribute to ϵ: the average plaquette and anti-plaquette occupation numbers. Depending on the prefactor $\lim_{\beta_G \to 0} \frac{1}{\beta_G} \left(\frac{\partial \xi}{\partial \beta} \right)^{-1}$, these observables could also give corrections to the results in the strong coupling limit. In the last chapter, we explored the Taylor expansion of the pressure in μ_B/T. We performed analytical crosschecks on small 2×2 lattices to form an expectation about the shape of the cumulants of the baryon density. Furthermore, we used exact enumerations in one dimension to predict the high temperature behaviour of the $3 + 1$d simulations. While the second order coefficient could be measured precisely, the fourth order turned out to be very noisy and the structure expected from the exact enumerations was replicated only vaguely. The reconstruction of the pressure with only the first two coefficients matched the direct simulations up to chemical potentials $a\mu_B = 0.9$. Beyond this value, the two methods begin to deviate from each other. Unfortunately, the achievable precision in the coefficients was not high enough to adress questions related to the critical endpoint. With higher statistics, strong coupling QCD might nethertheless provide an interesting testbed for the Taylor expansion method.

References

[1] Gert Aarts, Kirill Boguslavski, Manuel Scherzer, Erhard Seiler, Dénes Sexty, and Ion-Olimpiu Stamatescu. Getting even with CLE. *EPJ Web Conf.*, 175:14007, 2018.

[2] Christian Schmidt and Felix Ziesché. Simulating low dimensional QCD with Lefschetz thimbles. *PoS*, LATTICE2016:076, 2017.

[3] P. Rossi and U. Wolff. Lattice qcd with fermions at strong coupling: A dimer system. *Nuclear Physics B*, 248(1):105 – 122, 1984.

[4] F. Karsch and K.-H. Mütter. Strong coupling qcd at finite baryon-number density. *Nuclear Physics B*, 313(3):541 – 559, 1989.

[5] David H. Adams and Shailesh Chandrasekharan. Chiral limit of strongly coupled lattice gauge theories. *Nucl. Phys.*, B662:220–246, 2003.

[6] Giuseppe Gagliardi, Jangho Kim, and Wolfgang Unger. Dual Formulation and Phase Diagram of Lattice QCD in the Strong Coupling Regime. *EPJ Web Conf.*, 175:07047, 2018.

[7] Michael Edward Peskin and Daniel V. Schroeder. *An introduction to quantum field theory*. Advanced book program. Addison-Wesley, Reading, Mass. [u.a.], 2. print. edition, 1996.

[8] Kazuo Fujikawa and Hiroshi Suzuki. *Path integrals and quantum anomalies*, volume 122 of *International series of monographs on physics ; 122*. Clarendon Press, Oxford, repr. edition, 2005.

[9] Philippe de Forcrand, Wolfgang Unger, and Helvio Vairinhos. Strong-Coupling Lattice QCD on Anisotropic Lattices. *Phys. Rev.*, D97(3):034512, 2018.

[10] Jangho Kim and Wolfgang Unger. Quark Mass Dependence of the QCD Critical End Point in the Strong Coupling Limit. *PoS*, LATTICE2016:035, 2016.

[11] P. Hasenfratz and F. Karsch. Chemical Potential on the Lattice. *Phys. Lett.*, 125B:308–310, 1983.

[12] M. Fromm. *Lattice QCD at strong coupling: thermodynamics and nuclear physics*. PhD thesis, ETH Zürich, 2010.

[13] Christof Gattringer and Kurt Langfeld. Approaches to the sign problem in lattice field theory. *Int. J. Mod. Phys.*, A31(22):1643007, 2016.

[14] Philippe de Forcrand, Paul Romatschke, Wolfgang Unger, and Helvio Vairinhos. Thermodynamics of strongly-coupled lattice QCD in the chiral limit. *PoS*, LATTICE2016:086, 2017.

[15] Rajiv V. Gavai, Sourendu Gupta, and Swagato Mukherjee. Lattice quantum chromodynamics equation of state: A better differential method. *Pramana*, 71(3):487–508, Sep 2008.

[16] Philippe de Forcrand, Owe Philipsen, and Wolfgang Unger. QCD phase diagram from the lattice at strong coupling. *PoS*, CPOD2014:073, 2015.

[17] Philippe de Forcrand, Jens Langelage, Owe Philipsen, and Wolfgang Unger. Lattice QCD Phase Diagram In and Away from the Strong Coupling Limit. *Phys. Rev. Lett.*, 113(15):152002, 2014.

[18] A. Bazavov et al. Skewness and kurtosis of net baryon-number distributions at small values of the baryon chemical potential. *Phys. Rev.*, D96(7):074510, 2017.

[19] I. Montvay and G. Münster. *Quantum fields on a lattice*. Cambridge monographs on mathematical physics. Cambridge Univ. Press, Cambridge [u.a.], 1994.

[20] C. Gattringer and C. B. Lang. *Quantum chromodynamics on the lattice*, volume 788 of *Lecture notes in physics ; 788*. Springer, Berlin [u.a.], 2010.

[21] T. Muta. *Foundations of quantum chromodynamics*, volume 57 of *World Scientific lecture notes in physics ; 57*. World Scientific, Singapore [u.a.], 2. ed., reprint. edition, 2000.

A. Appendix

A.1. Additional plots

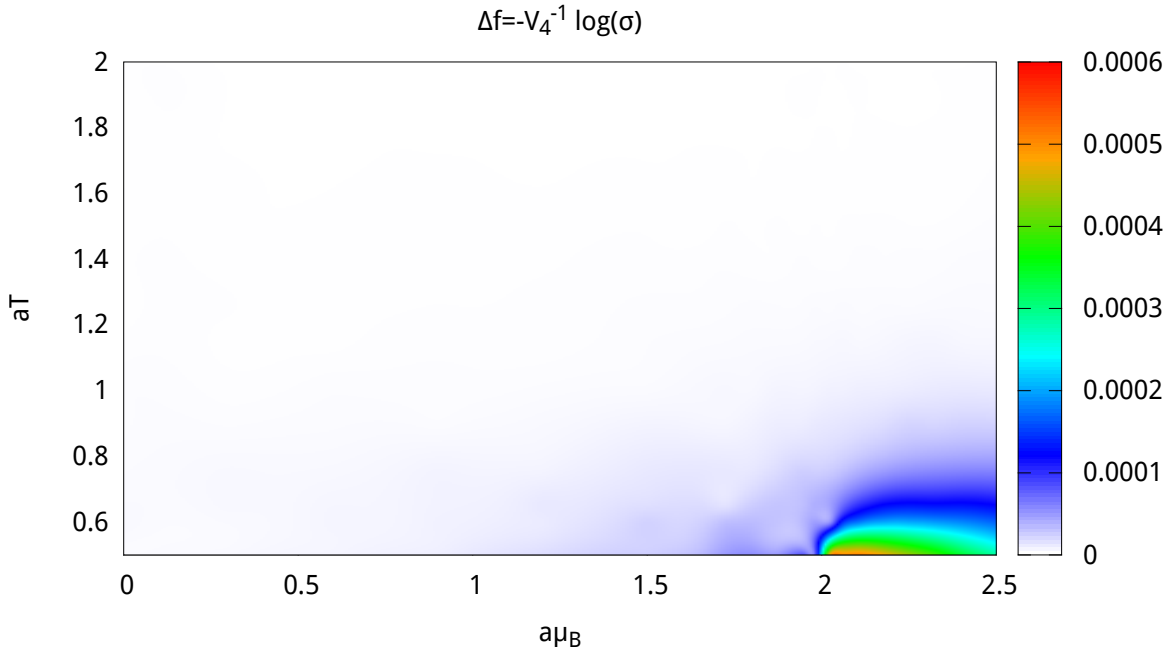

Figure 40: $\Delta f = -V^{-1} \log \sigma$ across the T, μ-plane for $am_q = 0.1$.

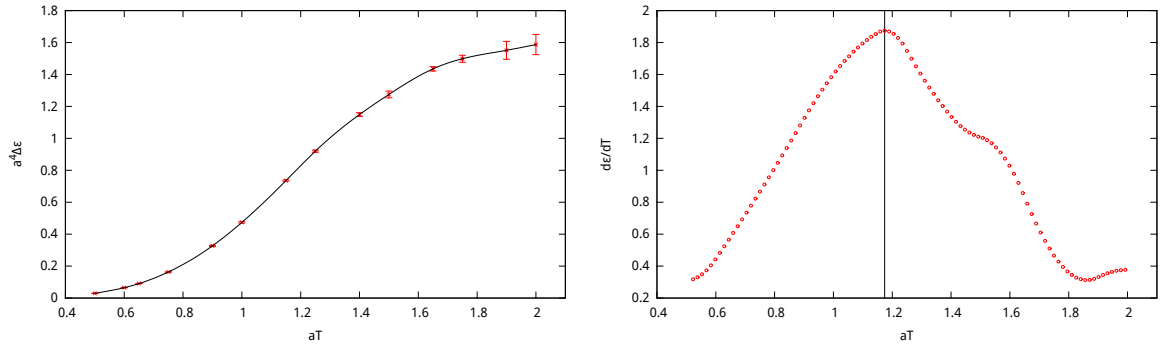

Figure 41: Interpolation of the energy density (left) and numerical derivative (right) to give a rough estimate of the crossover temperature used in section 7.

Eigenständigkeitserklärung

Hiermit erkläre ich, dass ich die vorliegende Arbeit selbstständig und nur unter Benutzung der angegebenen Hilfsmittel und Quellen verfasst habe. Die Stellen der Arbeit, die anderen Werken entnommen sind, habe ich unter Angabe der Quelle als Entlehnung kenntlich gemacht. Überdies erkläre ich, dass die vorliegende Arbeit noch nicht im Rahmen eines anderen Prüfungsverfahrens eingereicht wurde.

Bielefeld, den 26. September 2018 _____

Unterschrift